

Opacities for Photon Splitting and Pair Creation in Neutron Star Magnetospheres

Kun Hu,^{1*} Matthew G. Baring,¹ Zorawar Wadiasingh^{2,3} and Alice K. Harding²

¹*Department of Physics and Astronomy - MS 108, Rice University, 6100 Main Street, Houston, Texas 77251-1892, USA*

²*Gravitational Astrophysics Laboratory, Code 663, NASA's Goddard Space Flight Center, Greenbelt, MD 20770, USA*

³*Centre for Space Research, North-West University, Potchefstroom, South Africa*

Accepted 2019 April 5. Received 2019 April 3; in original form 2019 February 12.

ABSTRACT

Over the last four decades, persistent and flaring emission of magnetars observed by various telescopes has provided us with a suite of light curves and spectra in soft and hard X-rays, with no emission yet detected above around 1 MeV. Attenuation of such high-energy photons by magnetic pair creation and photon splitting is expected to be active in the magnetospheres of magnetars, possibly accounting for the paucity of gamma-rays in their signals. This paper explores polarization-dependent opacities for these two QED processes in static vacuum dipole magnetospheres of highly-magnetized neutron stars, calculating attenuation lengths and determining escape energies, which are the maximum photon energies for transparency out to infinity. The numerical trajectory integral analysis in flat and curved spacetimes provides upper bounds of a few MeV or less to the visible energies for magnetars for locales proximate to the stellar surface. Photon splitting opacity alone puts constraints on the possible emission locales in their magnetospheres: regions within field loops of maximum altitudes $r_{\max} \sim 2-4$ stellar radii are not commensurate with maximum detected energies of around 250 keV. These constraints apply not only to magnetar flares but also to their quiescent hard X-ray tail emission. An exploration of photon splitting attenuation in the context of a resonant inverse Compton scattering model for the hard X-ray tails derives distinctive phase-resolved spectroscopic and polarimetric signatures, of significant interest for future MeV-band missions such as AMEGO and e-ASTROGAM.

Key words: radiative transfer – radiation mechanisms: non-thermal – stars: magnetars – gamma-rays – X-rays – magnetic fields — polarization

1 INTRODUCTION

Magnetars are isolated neutron stars characterized by strong magnetic fields $\sim 10^{13} - 10^{15}$ G inferred from their rotational spin-down evolution, high persistent X-ray luminosities, and transient flaring activity in hard X-rays. Historically, magnetars have been categorized in two groups: soft gamma-ray repeaters (SGRs) and anomalous X-ray pulsars (AXPs). The magnetar scenario was first introduced by Duncan & Thompson (1992) for SGRs and later extended to AXPs by Thompson & Duncan (1996), wherein it was proposed that they are powered by the decay of magnetic fields. At present, around 30 magnetars have been observed – for a list of properties, see the McGill Magnetar Catalog (Olausen & Kaspi 2014) and its contemporaneous online version¹.

Magnetars evince bright, persistent pulsed X-ray emission, with luminosities often exceeding the rotational energy loss rate by several orders of magnitude; this disparity promotes the hypothesis that their strong magnetic fields power their emission. The soft X-ray spectra of magnetars can generally be fit by blackbody models with temperatures around 0.3–1 keV, connected to a steep power-law tail between 1 keV and 10 keV with an index around 2 to 4 (e.g., Mereghetti 2008; Viganò 2013; Turolla et al. 2015). The thermal component of the soft X-ray emission is believed to come from the surface of the star, while a leading model for the production of the non-thermal part is repeated resonant cyclotron scattering in a magnetospheric corona (e.g., Thompson, Lyutikov & Kulkarni 2002; Lyutikov & Gavriil 2006).

A third component of the persistent emission appears above 10 keV, fit with power-law models of an index between 1 to 2 (Kuiper et al. 2006; Götz et al. 2006; den Hartog et al. 2008a,b; Younes et al. 2017), i.e., much flatter than the soft X-ray spectra. These hard tails cannot extend much beyond a few hundred keV due to constraining upper bounds

* E-mail: kh38@rice.edu (KH); baring@rice.edu (MGB); zwadiasingh@gmail.com (ZW); ahardingx@yahoo.com (AKH)

¹ <http://www.physics.mcgill.ca/pulsar/magnetar/main.html>

obtained by COMPTEL at MeV energies and *Fermi*-LAT above 100 MeV (e.g., Abdo et al. 2010). Thus, a spectral break or turnover is indicated at around 200-700 keV, and a possible suggestion of this appears in *Fermi*-GBM spectra of 4U 0142+61 and 1E 1841-045 (ter Beek 2012). For this non-thermal hard X-ray component, resonant inverse Compton scattering is believed to be the most efficient radiative mechanism for its production (Baring & Harding 2007; Fernández & Thompson 2007; Beloborodov 2013; Wadiasingh et al. 2018). This process is resonant at the cyclotron frequency, increasing the cross section over the familiar non-magnetic Thomson value by around 2–3 orders of magnitude when $B \lesssim 4.4 \times 10^{13}$ Gauss (e.g., see Gonthier et al. 2000).

In addition to these quiescent signals, recurrent bursts of typical luminosities $10^{38} - 10^{42}$ erg/sec have been observed for many magnetars. Some episodes of such bursts last hours to days, over which tens to hundreds of individual short bursts can occur. The spectra of short bursts can be fit by a thermal bremsstrahlung model with temperatures around 30 keV (Gögüş et al. 1999, 2000; Feroci et al. 2004). In some sources a statistically better fit for burst spectra is obtained with a two-blackbody model (Israel et al. 2008; Lin et al. 2012; van der Horst et al. 2012; Younes et al. 2014), thereby promoting the possibility of thermal gradients existing in the magnetosphere.

Magnetars also exhibit giant flares of luminosities $10^{44} - 10^{47}$ erg/sec at hard X-ray energies extending up to around 1 MeV. They have been observed for only three SGRs (e.g., Mazets et al. 1979; Hurley et al. 1999, 2005), and for each of these, only once over roughly a 40 year period. They are characterized by a short, intense spike lasting for about 0.2 s. This peak count rate is then followed by an energetic pulsating tail lasting several minutes. The “fireball scenario” is the leading candidate in explaining the radiative dissipation and cooling phases of giant flares (e.g., Duncan & Thompson 1992; Thompson & Duncan 1995). In this picture, the energy released by the reconfiguration of crustal magnetic fields generates numerous electron-positron pairs in the magnetosphere. While much plasma flows out along the open field lines, an optically-thick pair fireball is trapped by the closed field lines for many rotation periods, both zones generating pulsating, cooling tails of giant flares. van Putten et al. (2016) determined that fireball-driven, high opacity outflows possess sufficient relativistic beaming to approximately yield the observed pulse fractions.

The upper bounds to energies of both quiescent and flare signals may be due to the intrinsic nature of plasma in the emission region, for example the effective temperature or mean Lorentz factor of the energetic pairs when heated by magnetic dissipation. Yet it is also suggestive of hard X-ray and gamma-ray attenuation in the magnetosphere, a prospect that is explored in this paper. Two exotic physical processes, magnetic pair creation and magnetic photon splitting, are expected to be effective in attenuating hard X-rays and gamma-rays in the magnetospheres of magnetars. One photon pair creation $\gamma \rightarrow e^\pm$ is permitted in strong-field environment because the external magnetic field can absorb momentum perpendicular to the field (e.g., Erber 1966). This process operates effectively for photons with energies above the absolute pair creation threshold of $2m_e c^2$. Below the pair threshold, magnetic photon splitting, a higher-order QED process (e.g., Adler 1971), can efficiently attenuate

high energy radiation. When the magnetic field strength exceeds around 10^{13} Gauss, these two processes generate opacity for high energy photons in the magnetospheres, perhaps helping explain the observed maximum energies and upper limits imposed by COMPTEL and *Fermi*-LAT.

Opacity calculations have been presented in a number of papers over the years. Baring (1995) discussed the spectral softening of SGR flares caused by repeated photon splitting. Harding, Baring & Gonthier (1996) computed attenuation lengths and escape energies for both pair creation and photon splitting for photons emergent from quasi-polar locales of neutron stars. Harding, Baring & Gonthier (1997) and Baring & Harding (2001) carried out cascade simulations incorporating splitting and pair creation in pulsar magnetospheres, discussing a possible “radio death line” for high-field pulsars (Baring & Harding 1998) caused by the suppression of pair creation. More recently, a detailed discussion on the pair creation opacity in neutron star magnetospheres was conducted by Story & Baring (2014). Their work, which focused mostly on emission from near the polar surface zones of neutron stars, used transparency criteria to constrain emission altitudes for gamma-ray pulsars in the context of *Fermi*-LAT and Čerenkov telescope observations.

In this paper, we calculate photon splitting and pair creation opacities in inner magnetospheres of neutron stars, applicable to arbitrary colatitudes and a substantial range of altitudes in closed field line zones above the stellar surface. The focus on these regions makes for a more pertinent connection with physical models of magnetar emission than was afforded with previous expositions. We present the attenuation lengths and escape energies as functions of emission position for photons emitted parallel or at small angles to the local magnetic fields. Starting from flat spacetime, we deliver opacity calculations both analytically and numerically. The numerical results here are in broad agreement with previous papers (Harding, Baring & Gonthier 1997; Baring & Harding 2001; Story & Baring 2014) that focus mainly on the polar cap region of neutron stars. Analytic approximations are deduced for photon splitting both to guide validation of the full numerical evaluations, and to supplement similar results offered in Story & Baring (2014) for pair creation.

Special emphasis is given to the case where photons are emitted along specific field loops, which is broadly applicable to models where high degrees of Doppler beaming are operable. In particular, comparatively simple empirical approximations for photon splitting and pair creation escape energies are provided for implementation in emission models explored elsewhere. As a case illustration, the opacity calculation is incorporated into the resonant inverse Compton scattering model of the hard X-ray tails to illustrate the phase-resolved spectroscopic and polarimetric characteristics for a spinning magnetar. This demonstrates the substantial variability of the maximum energy with pulse phase, helping to identify observational diagnostics that are possible with sensitive hard X-ray and Compton telescopes, both present and future. The influences of general relativity (GR) are discussed in Section 5, which are found to increase opacity in most parameter regimes, especially for emission directed inward. Therein, a “photosphere” plot is presented, where the opaque region in the magnetosphere for specific photon energy is depicted, and the main impact of GR in expanding the volume of opaque regions is clearly evident.

2 OPACITY GEOMETRY AND PHYSICS

To assess the importance of the photon splitting and pair creation in magnetars, the path-integrated opacity for these two processes is calculated. From these are derived two central quantities, the attenuation length and the escape energy. Before developing the opacity calculations, the essentials of the geometry and the quantum physics are outlined in this Section.

2.1 Radiative Transfer Geometry

For opacity determination, a test photon is presumed to be emitted from a specific location with an altitude r_E and a polar colatitude θ_E in the magnetosphere of a neutron star. The photon then propagates in the direction of its momentum vector which makes an angle δ_E with respect to its emission location vector \mathbf{r}_E . The optical depth for the splitting of photons and for pair creation takes the form of a trajectory integral:

$$\tau(l) = \int_0^l \mathcal{R} ds \quad , \quad (1)$$

where \mathcal{R} is the attenuation coefficient in units of cm^{-1} and l is the cumulative path length along the photon trajectory out to some observation point, ds being the differential path length. The emission and propagation geometry is depicted in Fig. 1. The *attenuation length* L is defined to be the path length over which the optical depth equals unity:

$$\tau(L) = \int_0^L \mathcal{R} ds = 1 \quad . \quad (2)$$

Since \mathcal{R} is generally a strongly increasing function of photon energy ε , $\tau(\infty) < 1$ domains can be realized when ε is below some critical value. This criterion defines the *escape energy* ε_{esc} : it is the energy at which the attenuation length becomes infinity, so that photons with lower energies escape the magnetosphere of the star. Thus the escape energy demarcates the boundary between transparency and opacity of the magnetosphere, a signature role that is identified in Harding, Baring & Gonthier (1997); Baring & Harding (2001) and references therein.

In Sections 3 and 4, only flat spacetime propagation is treated in our considerations of photon attenuation. This approximation is generally applicable for emission at moderate or high altitudes. Yet for emission locales within 1-2 stellar radii of the surface, general relativistic (GR) influences become important. The main ones are curved photon trajectories, gravitational redshift, the deformation of the dipole field and concomitant changes in field strengths, all of which will be addressed in Section 5, wherein ds will represent coordinate length along a geodesic. GR effects will perturb the results obtained in Sections 3 and 4. Yet, Minkowski spacetime considerations provide important insights into the characteristics of photon attenuation, and facilitate the derivation of useful analytic approximations.

The flat spacetime geometry of the photon trajectory is illustrated in the left panel of Fig. 1. Throughout, a vacuum dipole magnetic field is assumed, with a polar coordinate representation

$$\mathbf{B} = \frac{B_p R_{NS}^3}{2r^3} \left(2 \cos \theta \hat{\mathbf{r}} + \sin \theta \hat{\boldsymbol{\theta}} \right) \quad , \quad (3)$$

where the angle θ represents the magnetic colatitude. Here B_p is the surface polar (when $\theta = 0$) magnetic field strength and R_{NS} is the radius of the star. Throughout this paper, we assume $R_{NS} = 10^6$ cm. The dipole assumption is a convenient choice, suited to attenuation processes that take place at low altitude: since magnetars are generally slow rotators, rotational aberration influences are small. Departures from dipolar morphology as imbued in twisted magnetospheres (e.g., Thompson, Lyutikov & Kulkarni 2002; Chen & Beloborodov 2017) will alter the computed photon opacities somewhat; the extent to which they modify the overall character of the results presented below, if at all, is deferred to future work.

2.1.1 Coordinate Bases and the Photon Momentum \mathbf{k}

We now identify three groups of coordinate bases to describe the trajectory of photons: (i) $\{\hat{\mathbf{x}}, \hat{\mathbf{y}}, \hat{\mathbf{z}}\}$ is a right-handed coordinate system with an origin at the star's center, its z-axis coinciding with the magnetic axis of the star and the emission point of the photon (without loss of generality) lying in the $x - z$ plane – it applies to any point on the photon path; (ii) $\{\hat{\mathbf{r}}, \hat{\boldsymbol{\theta}}, \hat{\boldsymbol{\phi}}\}$ is the corresponding spherical polar coordinate system at any location in the path, and (iii) $\{\hat{\mathbf{r}}_E, \hat{\boldsymbol{\theta}}_E, \hat{\boldsymbol{\phi}}_E\}$ is the particular spherical polar coordinate system that applies specifically to the emission point. Obviously, the polar coordinate system (ii) is most suited to describing the magnetic field structure, while the emission point polar system (iii) is advantageous when specifying the direction of the photon trajectory. The relations between the Cartesian and emission point polar coordinates are

$$\begin{aligned} \hat{\mathbf{x}} &= \sin \theta_E \hat{\mathbf{r}}_E + \cos \theta_E \hat{\boldsymbol{\theta}}_E \quad , \\ \hat{\mathbf{y}} &= \hat{\boldsymbol{\phi}}_E \quad , \\ \hat{\mathbf{z}} &= \cos \theta_E \hat{\mathbf{r}}_E - \sin \theta_E \hat{\boldsymbol{\theta}}_E \quad , \end{aligned} \quad (4)$$

with an analogous system of identities for general positions along the path. One can then express the unit momentum vector \mathbf{k} of the emitted photon in terms of coordinates at the emission point:

$$\mathbf{k} = \cos \delta_E \hat{\mathbf{r}}_E + \sin \delta_E \cos \omega_E \hat{\boldsymbol{\theta}}_E + \sin \delta_E \sin \omega_E \hat{\boldsymbol{\phi}}_E \quad . \quad (5)$$

In the absence of GR modifications, the vector \mathbf{k} is a constant along the photon path. In this expression, δ_E is the angle between \mathbf{k} and the radial direction at the emission point (see the left panel of Fig. 1), and ω_E is an azimuth angle at the emission point relative to the $\hat{\mathbf{x}} - \hat{\mathbf{z}}$ plane, as illustrated in the right panel of Fig. 1. Specifically,

$$\cos \omega_E = \frac{\mathbf{k} \cdot \hat{\boldsymbol{\theta}}_E}{\sin \delta_E} \quad . \quad (6)$$

For flat spacetime propagation, the position vector \mathbf{r} along the path is given by $\mathbf{r} = r_E \hat{\mathbf{r}}_E + s \mathbf{k}$, where s is the path length of the photon trajectory.

A sometimes advantageous rearrangement of the emission locale coordinates can be realized by rotating in the $\hat{\mathbf{r}}_E - \hat{\boldsymbol{\theta}}_E$ plane to align one basis axis with the magnetic

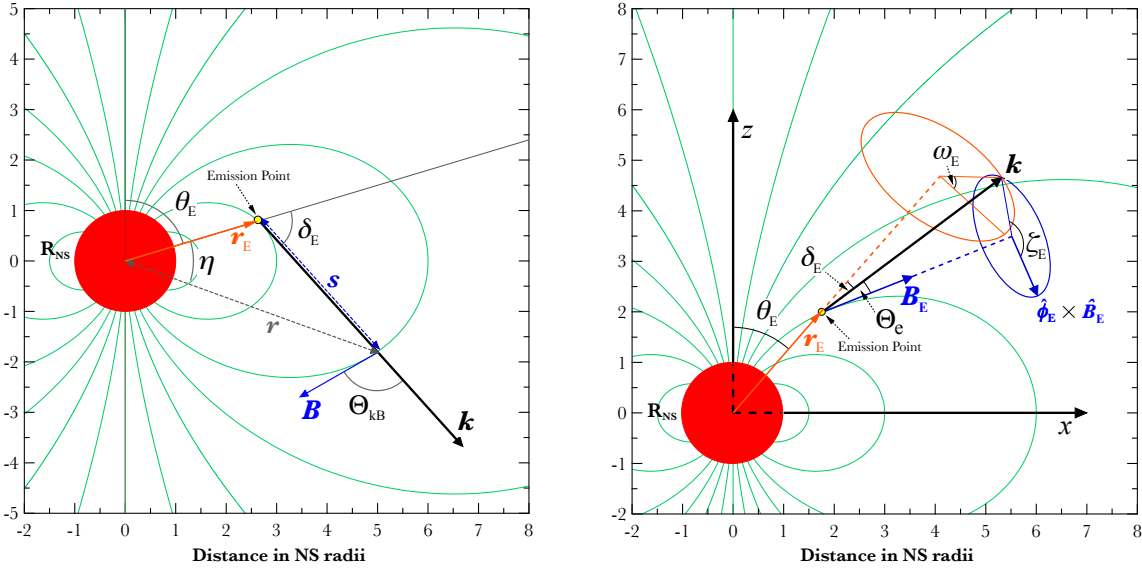


Figure 1. *Left Panel:* Photon propagation geometry in a dipole magnetic field, with green curves representing field lines, specifically for meridional cases in the $x - z$ plane where the light path is coplanar with the field loops. The photon emission point is at an altitude $r_E = hR_{\text{NS}}$ and colatitude θ_E . The photon trajectory, represented by the black line, is a straight line for Euclidean geometry; a curved path (not shown here) applies for general relativistic considerations. At any location along the photon path, \mathbf{k} is the photon momentum vector, and \mathbf{B} is the local magnetic field vector; the angle between these two vectors is Θ_{kB} , given in Eq. (19). All such locations are defined by the propagation angle η , with the radial position r relative to the center of the neutron star, and the distance s from the point of emission being related via Eq. (12). *Right Panel:* Geometry pertinent to the trajectory at the point of photon emission, for cases where \mathbf{B} and \mathbf{k} do not necessarily lie in the meridional $x - z$ plane, which is also the $(\hat{\mathbf{B}}_E, \hat{\phi}_E \times \hat{\mathbf{B}}_E)$ plane. The magnetic field vector \mathbf{B}_E at the emission point is also displayed. Here, δ_E is the angle between \mathbf{k} and \mathbf{r}_E , the radial vector at the point of emission, and ω_E is the azimuth angle with respect to the $\hat{\theta}_E$ vector at this point, given in Eq. (6). In addition, Θ_e is the angle between \mathbf{k} and $\hat{\mathbf{B}}_E$, and ζ_E is the azimuth angle around $\hat{\mathbf{B}}_E$ with respect to the $\hat{\phi}_E \times \hat{\mathbf{B}}_E$ vector at the emission location. Either (δ_E, ω_E) or (Θ_e, ζ_E) determine the photon propagation direction, and relations between them are given in Eqs. (9) and (10).

field direction. This can be encapsulated in the identities

$$\begin{aligned} \hat{\mathbf{r}}_E &= \frac{1}{\sqrt{3 \cos^2 \theta_E + 1}} \left[2 \cos \theta_E \hat{\mathbf{B}}_E - \sin \theta_E (\hat{\phi}_E \times \hat{\mathbf{B}}_E) \right], \\ \hat{\theta}_E &= \frac{1}{\sqrt{3 \cos^2 \theta_E + 1}} \left[\sin \theta_E \hat{\mathbf{B}}_E + 2 \cos \theta_E (\hat{\phi}_E \times \hat{\mathbf{B}}_E) \right]. \end{aligned} \quad (7)$$

The vectors $\hat{\mathbf{B}}_E$ and $\hat{\phi}_E \times \hat{\mathbf{B}}_E$ are marked on the right panel of Fig. 1. Using this choice, one can specify the photon momentum vector \mathbf{k} at the emission point in terms of a $\{\hat{\mathbf{B}}_E, \hat{\phi}_E, \hat{\phi}_E \times \hat{\mathbf{B}}_E\}$ basis. This can be completed by inserting Eq. (7) into Eq. (5), though the explicit result is not displayed here. An alternative is to employ the angle Θ_e between \mathbf{k} and $\hat{\mathbf{B}}_E$ and the azimuthal angle ζ_E with respect to $\hat{\phi}_E \times \hat{\mathbf{B}}_E$ in a spherical triangle construction. These two angles are depicted in Fig. 1. Then one has

$$\mathbf{k} = \cos \Theta_e \hat{\mathbf{B}}_E + \sin \Theta_e \cos \zeta_E (\hat{\phi}_E \times \hat{\mathbf{B}}_E) + \sin \Theta_e \sin \zeta_E \hat{\phi}_E. \quad (8)$$

Equating the coefficients of this expression with those of the form obtained from Eq. (5) using the substitution captured in Eq. (7) yields

$$\begin{aligned} \cos \delta_E = \mathbf{k} \cdot \hat{\mathbf{r}}_E &= \frac{2 \cos \Theta_e \cos \theta_E - \sin \Theta_e \cos \zeta_E \sin \theta_E}{\sqrt{3 \cos^2 \theta_E + 1}}, \\ \cos \omega_E = \frac{\mathbf{k} \cdot \hat{\theta}_E}{\sin \delta_E} &= \frac{2 \cos \Theta_e \sin \theta_E + \sin \Theta_e \cos \zeta_E \cos \theta_E}{\sin \delta_E \sqrt{3 \cos^2 \theta_E + 1}} \end{aligned} \quad (9)$$

from the basis vectors in the meridional $(\hat{\mathbf{B}}_E, \hat{\phi}_E \times \hat{\mathbf{B}}_E)$ plane. To these can be added a third identity pertaining

to the $\hat{\phi}_E$ direction:

$$\sin \delta_E \sin \omega_E = \sin \Theta_e \sin \zeta_E. \quad (10)$$

These three relations can prove useful in expressing key results just below.

2.1.2 Relative direction of the Photon \mathbf{k} and the Field \mathbf{B}

In Section 2.2 it will become evident that the attenuation coefficients for the quantum processes considered here are critically sensitive to the angle Θ_{kB} between the momentum of the photon at any point on its trajectory and the local magnetic field. This angle is given by

$$\cos \Theta_{\text{kB}} = \frac{\mathbf{k} \cdot \mathbf{B}}{|\mathbf{B}|} \quad \text{or} \quad \sin \Theta_{\text{kB}} = \frac{|\mathbf{k} \times \mathbf{B}|}{|\mathbf{B}|}, \quad (11)$$

noting that $|\mathbf{k}| = 1$. We seek an expression for this angle in terms of the polar angles θ, ϕ at points along the path, the pathlength s , and the emission locale parameters (r_E, θ_E) and direction parameters (δ_E, ω_E) . Since \mathbf{k} is fixed, the direction of the field at each locale along the trajectory determines the value of Θ_{kB} . This angle can be expressed using local polar coordinates (r, θ, ϕ) along its trajectory. The distance from the star center is

$$r \equiv |\mathbf{r}| = |\mathbf{r}_E + s\mathbf{k}| = \sqrt{r_E^2 + s^2 + 2sr_E \cos \delta_E}, \quad (12)$$

which is quickly gleaned from Fig. 1. Similarly, one can express the **propagation angle** η depicted in the left panel of Fig. 1 using the cosine or sine rules:

$$\cos \eta = \frac{r^2 + r_E^2 - s^2}{2rr_E}, \quad \sin \eta = \frac{s}{r} \sin \delta_E. \quad (13)$$

These definitions apply regardless of whether or not the propagation vector \mathbf{k} is co-planar with magnetic field loops. This angle will prove useful for the development of analytic asymptotic approximations in due course, serving as an alternative to the pathlength variable s . At the point of emission, $\eta = 0$. As $r \rightarrow \infty$ out to an observer, \mathbf{k} becomes essentially parallel to the local radial vector \mathbf{r} , and $\eta \rightarrow \delta_E$: see the left panel of Fig. 1 or Eq. (5).

Expressions for the two polar coordinate angles contain more involved geometrical algebra. Given that $\mathbf{r} = r_E \hat{\mathbf{r}}_E + s \mathbf{k}$, using Eqs. (4) and (5) the polar angle (magnetic colatitude) can be expressed via

$$\begin{aligned} \cos \theta &= \frac{\mathbf{r} \cdot \hat{\mathbf{z}}}{r} \\ &= \frac{(r_E + s \cos \delta_E) \cos \theta_E - s \sin \delta_E \cos \omega_E \sin \theta_E}{\sqrt{r_E^2 + s^2 + 2sr_E \cos \delta_E}}. \end{aligned} \quad (14)$$

One could form a result using $\sin \theta = |\mathbf{r} \times \hat{\mathbf{z}}|/r$. Yet, in practice, only a form for $r^2 \sin^2 \theta$ is needed, and this is routinely obtained from Eq. (14). The azimuthal angle or magnetic longitude is encapsulated in the relation

$$\begin{aligned} r_x &\equiv \mathbf{r} \cdot \hat{\mathbf{x}} = r \sin \theta \cos \phi \\ &= (r_E + s \cos \delta_E) \sin \theta_E + s \sin \delta_E \cos \omega_E \cos \theta_E. \end{aligned} \quad (15)$$

The alternative relation for ϕ is

$$r_y \equiv \mathbf{r} \cdot \hat{\mathbf{y}} = r \sin \theta \sin \phi = s \sin \delta_E \sin \omega_E; \quad (16)$$

both forms can be employed in Eq. (19) below to eliminate the explicit dependence on ϕ . Observe that forming the dot product using the perpendicular axes $\hat{\mathbf{x}}$ and $\hat{\mathbf{y}}$ is the most convenient path to isolating these identities for the projections of \mathbf{r} onto the (x, y) -plane. Summing the squares of Eqs. (15) and (16) yields the form for $r_x^2 + r_y^2 = r^2 \sin^2 \theta$. Then adding to this $r^2 \cos^2 \theta$ using Eq. (14) and equating to the value of r^2 obtained from Eq. (12) generates spherical trigonometric relations between δ_E , θ_E and ω_E to close the group of geometric identities.

To express the magnetic field in Eq. (3) we now have forms for two basis vectors, namely the radial direction

$$\hat{\mathbf{r}} = \frac{r_E \hat{\mathbf{r}}_E + s \mathbf{k}}{\sqrt{r_E^2 + s^2 + 2sr_E \cos \delta_E}}, \quad (17)$$

where \mathbf{k} is written in Eq. (5), and the polar angle direction

$$\begin{aligned} \hat{\boldsymbol{\theta}} &= (\sin \theta_E \cos \theta \cos \phi - \cos \theta_E \sin \theta) \hat{\mathbf{r}}_E \\ &\quad + (\cos \theta_E \cos \theta \cos \phi + \sin \theta_E \sin \theta) \hat{\boldsymbol{\theta}}_E \\ &\quad + \cos \theta \sin \phi \hat{\boldsymbol{\phi}}_E. \end{aligned} \quad (18)$$

This second vector is obtained from the $\{\hat{\mathbf{r}}_E, \hat{\boldsymbol{\theta}}_E, \hat{\boldsymbol{\phi}}_E\}$ triad via a rotation through $\theta - \theta_E$ about the y axis followed by a rotation through ϕ about the z -axis. Then, selecting the dot product form in Eq. (11), one can evaluate $\cos \Theta_{\text{KB}}$ as

$$\begin{aligned} \cos \Theta_{\text{KB}} &= \frac{1}{\sqrt{3 \cos^2 \theta + 1}} \left[2 \cos \theta \left(\frac{r_E \cos \delta_E + s}{r} \right) \right. \\ &\quad + \sin \theta \cos \delta_E (\sin \theta_E \cos \theta \cos \phi - \cos \theta_E \sin \theta) \\ &\quad + \sin \theta \sin \delta_E \cos \omega_E (\cos \theta_E \cos \theta \cos \phi + \sin \theta_E \sin \theta) \\ &\quad \left. + \sin \theta \sin \delta_E \sin \omega_E \cos \theta \sin \phi \right]. \end{aligned} \quad (19)$$

Converting Eq. (19) into a sine, one can then compute the attenuation opacity at any point of the photon trajectory, using the relativistic quantum forms for the attenuation rates expounded in Section 2.2.

A case of particular interest is that where photons propagate in the plane of a set of field loops, termed the **meridional plane**, a situation that is depicted in the left panel of Fig. 1. This is fairly representative of general expectations because in most models of pulsar and magnetar hard X-ray and gamma-ray emission, the photons are created by ultra-relativistic electrons moving essentially along field lines, at least at low magnetospheric altitudes. One can therefore set $\phi = 0$. Doppler aberration for $\gamma_e \gg 1$ circumstances generates very small angles $\Theta_e \lesssim 1/\gamma_e \ll 1$ between the photon momentum vector and the magnetic field at the point of emission. Thus, Θ_{KB} normally starts at very small values, and increases as the photon propagates. In cases where photons are emitted exactly parallel to the local field line, i.e., $\Theta_e = 0$, one can set $\omega_E = 0$, and it then follows that $2 \tan \delta_E = \tan \theta_E$. Then the algebra for the angle Θ_{KB} simplifies dramatically, yielding the forms

$$\begin{aligned} \cos \Theta_{\text{KB}} &= \frac{\sin \theta \sin(\delta_E - \eta) + 2 \cos \theta \cos(\delta_E - \eta)}{\sqrt{3 \cos^2 \theta + 1}} \\ \sin \Theta_{\text{KB}} &= \frac{\sin \theta \cos(\delta_E - \eta) - 2 \cos \theta \sin(\delta_E - \eta)}{\sqrt{3 \cos^2 \theta + 1}}, \end{aligned} \quad (20)$$

remembering that $\eta = \theta - \theta_E$ in this special meridional case. This result reproduces Eq. (14) of Story & Baring (2014). Observe that here Θ_{KB} is independent of the r coordinate because of the self similarity of the dipole field configuration that is sampled for propagation in planes containing field loops; in general, Θ_{KB} is dependent on r – see Eq. (19).

2.2 Photon Splitting and Pair Creation Physics

Having outlined the geometrical construction pertinent to the propagation calculation, now the key results for the attenuation coefficients \mathcal{R} for the two quantum processes under consideration, photon splitting $\gamma \rightarrow \gamma\gamma$ and pair creation $\gamma \rightarrow e^+e^-$, are summarized. Extensive discussion of the two processes is provided in Harding, Baring & Gonthier (1997); Baring & Harding (2001); Harding & Lai (2006), and references therein, so here a briefer exposition suffices.

Magnetic photon splitting is a third-order QED process in which a single photon splits into two lower-energy photons Adler (1971); Baring & Harding (1997). It is forbidden in the absence of an external field due to a charge conjugation symmetry (Furry's theorem) concerning propagators in the triangular Feynman diagram, and becomes possible as the field breaks this symmetry. It operates efficiently and competes effectively with one photon (magnetic) pair production in magnetic fields above $\sim 10^{13}$ Gauss (Harding, Baring & Gonthier 1997) because it has no mass/energy threshold, and so can attenuate hard X-rays, typically in the 50-500 keV band. The magnetized vacuum is dispersive and birefringent, so that the refractive index deviates slightly from unity, and the phase velocity of light is less than c and depends on the polarization state of photons. The physics of this vacuum dispersion is addressed extensively in Adler (1971) and Shabad (1975), and we note that the directions

of the resultant photons are almost but not quite co-linear with that of the attenuated photon. In the limit of very weak dispersion, there are three polarization modes of splitting that are permitted by the CP (charge-parity) invariance in QED: $\perp \rightarrow \parallel\parallel$, $\parallel \rightarrow \perp\perp$ and $\perp \rightarrow \perp\perp$. Here, as in many previous papers, we adopt the linear polarization convention for light where \parallel (ordinary or O-mode) refers to the state with the photon's *electric* field vector parallel to the plane containing the magnetic field \mathbf{B} and the photon's momentum vector (i.e., \mathbf{k}), while \perp (extraordinary or X-mode) denotes the photon's electric field vector being normal to this plane.

Adler (1971) observed that in order to conserve both energy and momentum, the influence of vacuum dispersion was to restrict $\gamma \rightarrow \gamma\gamma$ to the $\perp \rightarrow \parallel\parallel$ mode below pair production threshold, and prohibit the other two CP-permitted channels, *kinematic selection rules* that can potentially seed strong polarization of X-ray spectra. This result was derived in the weak, linear domain assuming that magnetized vacuum contributions dominate the dispersion relation, wherein pair creation $\gamma \rightarrow e^+e^-$ is the dominant absorptive process. In highly super-critical fields, quadratic and higher order resonant contributions to the generalized vacuum polarizability tensor may modify this result. In parallel, when plasma densities are high, or very near the cyclotron resonance, plasma dispersion competes with the magnetic vacuum contribution, thereby modifying both the propagation characteristics and the splitting selection rules. The competition between vacuum and plasma dispersion spawns the so-called vacuum resonance (e.g., see Mészáros 1992, and references therein), at which polarization states for photons are modified in magnetized media with strong density gradients. Examples for sites sampling the vacuum resonance include accretion columns in X-ray pulsars (e.g., Mészáros & Ventura 1978; Gnedin et al. 1978) and the surface layers of magnetars (e.g., Özel 2001; Lai & Ho 2003). While we provide here forms for all three CP-permitted splitting rates, throughout much of the ensuing exposition, it will be assumed that Adler's kinematic selection rules apply, yielding an emphasis on results for $\perp \rightarrow \parallel\parallel$ splittings.

Fully general expressions for photon splitting rates are mathematically complicated, and usually not required. S-matrix determinations of the rates provided in Baring (2000) involve triple summations of combinations of elementary functions over the Landau level quantum numbers of virtual electrons. Euler-Heisenberg formulations are offered in Adler (1971), and these incorporate triple integrals. In the low-energy limit well below the pair creation threshold of $\varepsilon \sin \Theta_{\text{kB}} = 2$ (hereafter, all photon energies are expressed dimensionlessly, scaled by $m_e c^2$), comparatively simple, single-integral expressions are obtainable because the energy and magnetic field dependences of the splitting amplitudes become separable. These are the forms employed here. To express them, we introduce two functions that serve as reaction amplitude coefficients, \mathcal{M}_1 , \mathcal{M}_2 defined by

$$\mathcal{M}_\sigma = \frac{1}{B^4} \int_0^\infty \frac{ds}{s} e^{-s/B} \Lambda_\sigma(s) \quad , \quad (21)$$

where

$$\begin{aligned} \Lambda_1(s) &= \left(-\frac{3}{4s} + \frac{s}{6} \right) \frac{\cosh s}{\sinh s} + \frac{3 + 2s^2}{12 \sinh^2 s} + \frac{s \cosh s}{2 \sinh^3 s} \quad , \\ \Lambda_2(s) &= \frac{3 \cosh s}{4s \sinh s} + \frac{3 - 4s^2}{4 \sinh^2 s} - \frac{3s^2}{2 \sinh^4 s} \quad , \end{aligned} \quad (22)$$

forms that were first identified by Adler (1971). In these integrals, and throughout this paper, the magnetic field B is expressed in dimensionless form, being scaled by the quantum critical field $B_{\text{cr}} = m_e^2 c^3 / (e\hbar) \approx 4.41 \times 10^{13}$ Gauss, at which the electron cyclotron and rest mass energies are equal. In the limit of $B \ll 1$, $\mathcal{M}_1 \approx 26/315$ and $\mathcal{M}_2 \approx 16/105$ are both independent of the field strength, while for highly-supercritical fields, $B \gg 1$, one can quickly determine that $\mathcal{M}_1 \approx 1/(6B^3)$ and $\mathcal{M}_2 \approx 1/(3B^4)$. Since the splitting rates are proportional to the $(\mathcal{M}_\sigma)^2$, it is apparent that the \mathcal{M}_σ constitute strong-field modification factors.

The approximate splitting rates can be scaled by $1/c$ and thereby expressed as inverse attenuation lengths, i.e., *attenuation coefficients* \mathcal{R}^{sp} , using these two functions. For the 3 CP-permitted modes, photons of dimensionless energy ε propagating at angle Θ_{kB} to the local field direction have coefficients

$$\begin{aligned} \mathcal{R}_{\perp \rightarrow \parallel\parallel}^{\text{sp}} &= \frac{\alpha_f^3}{60\pi^2 \lambda_c} \varepsilon^5 B^6 \mathcal{M}_1^2 \sin^6 \Theta_{\text{kB}} = \frac{1}{2} \mathcal{R}_{\parallel \rightarrow \perp\perp}^{\text{sp}} \quad , \\ \mathcal{R}_{\perp \rightarrow \perp\perp}^{\text{sp}} &= \frac{\alpha_f^3}{60\pi^2 \lambda_c} \varepsilon^5 B^6 \mathcal{M}_2^2 \sin^6 \Theta_{\text{kB}} \quad . \end{aligned} \quad (23)$$

These forms are integrated over the energies of the produced photons, which sum to $\varepsilon m_e c^2$. Here $\alpha_f = e^2/\hbar c$ is the fine-structure constant, and $\lambda_c = \hbar/m_e c$ is the reduced Compton wavelength of the electron. The $\Theta_{\text{kB}} = \pi/2$ specialization of Eq. (23) is listed in Baring & Harding (2001), and the $\sin^6 \Theta_{\text{kB}}$ angle dependence captures Lorentz transformation properties for boosts along \mathbf{B} in this special $\varepsilon \sin \Theta_{\text{kB}} \ll 2$ case. Observe that the $1/2$ factor multiplying $\mathcal{R}_{\parallel \rightarrow \perp\perp}^{\text{sp}}$ in Eq. (23) accounts for the two possibilities $\parallel \rightarrow \perp\perp$ and $\parallel \rightarrow \parallel\perp$, which have identical rates (see Eq. (23) of Adler 1971); thus this first relation encapsulates crossing symmetries for splitting. The strong dependence on ε guarantees that photon splitting can be very effective at attenuating soft gamma-rays provided that Θ_{kB} is not small. For unpolarized photons, Eq. (23) can be averaged to yield

$$\mathcal{R}_{\text{ave}}^{\text{sp}} = \frac{\alpha_f^3}{120\pi^2 \lambda_c} \varepsilon^5 B^6 \left(3\mathcal{M}_1^2 + \mathcal{M}_2^2 \right) \sin^6 \Theta_{\text{kB}} \quad . \quad (24)$$

Such a form is useful if all three CP-permitted modes of splitting are assumed to operate, in which repeated splittings are possible, and a splitting cascade can develop, producing numerous photons of lower energy with potentially discernible spectral bumps near the escape energy: see Baring (1995); Harding & Baring (1996); Harding, Baring & Gonthier (1997). Note also that for $\varepsilon \sin \Theta_{\text{kB}} \lesssim 2$ near the pair threshold, Baring & Harding (1997) provided a compact, empirical approximation to the attenuation coefficient for the $\perp \rightarrow \parallel\parallel$ mode.

One-photon pair production $\gamma \rightarrow e^+e^-$ is a first-order QED process that is forbidden in field-free regions because four-momentum cannot be conserved. An external magnetic field can absorb momentum perpendicular to \mathbf{B} , and so the pair conversion of a single photon can proceed. Early determinations of the rate by Toll (1952) and Klepikov (1954) revealed that it rises exponentially with increasing photon energy and magnetic field strength, becoming significant for gamma-rays above the absolute threshold, $\varepsilon = 2/\sin \Theta_{\text{kB}}$, and for fields approaching B_{cr} . This threshold applies to the parallel (\parallel) polarization, with that for the \perp polarization being a factor of $1 + \sqrt{1 + 2B}$ higher: see Eq. (31).

In general, the produced pairs occupy excited Landau levels in a magnetic field, and for each Landau level configuration of the pairs, the attenuation coefficient \mathcal{R}^{PP} for the reaction exhibits a divergent resonance at each pair state threshold, producing a characteristic sawtooth structure (e.g., Daugherty & Harding 1983; Baier & Katkov 2007). These mathematically-complicated forms involve sums over associated Laguerre functions and are often unwieldy in numerical analyses such as opacity computations. As the divergences are integrable in the photon energy dimension, mathematical approximations to the rate can be developed using proper-time techniques originally due to Schwinger (1951) that effectively average over ranges of ε somewhat broader than the separation of neighboring resonances. The most widely-used expressions of this genre are those derived in Klepikov (1954), Erber (1966) and Tsai & Erber (1974); see also the book of Sokolov & Ternov (1968). When expressed as attenuation coefficients, they assume the form

$$\mathcal{R}_{\parallel,\perp}^{\text{PP}} = \frac{\alpha_f}{\lambda_c} B \sin \Theta_{\text{KB}} \mathcal{F}_{\parallel,\perp}(\varepsilon_{\perp}, B), \quad \varepsilon_{\perp} = \varepsilon \sin \Theta_{\text{KB}}. \quad (25)$$

As in Eq. (23), covariant structure under Lorentz boosts parallel to \mathbf{B} is apparent, since $\varepsilon_{\perp} = \varepsilon \sin \Theta_{\text{KB}}$ is a conserved quantity under such transformations. Thus, the appearance of the extra $\sin \Theta_{\text{KB}}$ factor captures time dilation or length contraction information in such boosts. The specific forms first obtained by Erber (1966) were

$$\mathcal{F}_{\perp} = \frac{1}{2} \mathcal{F}_{\parallel} = \frac{2}{3} \mathcal{F}_{\text{Erber}}, \quad (26)$$

$$\mathcal{F}_{\text{Erber}}(\varepsilon_{\perp}, B) = \frac{3\sqrt{3}}{16\sqrt{2}} \exp\left(-\frac{8}{3\varepsilon_{\perp}B}\right).$$

These are applicable when the produced pairs are in high Landau states, namely when $\varepsilon_{\perp}^2/2B \gg 1$ and $\varepsilon_{\perp} \gg 1$. Integrated over the momenta of the produced pairs, these are valid only in the domain $\varepsilon_{\perp}B \lesssim 0.1$, for which the pairs are ultra-relativistic, and the exponential factor introduces a profound sensitivity to the values of ε , B and Θ_{KB} . The approximations in Eq. (26) become inaccurate near the pair threshold of $\varepsilon_{\perp} = 2$, a domain that is important in fields $B \gtrsim 0.5$, as pointed out by Baring & Harding (2001). Nevertheless, they are often extremely useful, and have been employed widely in the pulsar literature, including in the seminal papers of Sturrock (1971); Ruderman & Sutherland (1975) and Daugherty & Harding (1982).

For the purposes of opacity determinations, it is necessary to employ improvements of the asymptotic formulae in Eq. (26) that accommodate reduced rates for pair production near threshold. Here we adopt the protocol of Story & Baring (2014), who used the analysis of threshold corrections provided by Baier & Katkov (2007), specifically their Eq. (3.4), yielding the form

$$\mathcal{F}_{\text{TH}}(\varepsilon_{\perp}, B) = \frac{3\varepsilon_{\perp}^2 - 4}{2\varepsilon_{\perp}^2 \sqrt{\mathcal{L}(\varepsilon_{\perp}) \phi(\varepsilon_{\perp})}} \exp\left\{-\frac{\phi(\varepsilon_{\perp})}{4B}\right\}, \quad (27)$$

valid for $\varepsilon_{\perp} > 2$, where $\phi(\varepsilon_{\perp}) = 4\varepsilon_{\perp} - \mathcal{L}(\varepsilon_{\perp})$ and

$$\mathcal{L}(\varepsilon_{\perp}) = (\varepsilon_{\perp}^2 - 4) \log_e \left(\frac{\varepsilon_{\perp} + 2}{\varepsilon_{\perp} - 2} \right). \quad (28)$$

This analytic result improves upon the Erber form in

Eq. (26) by several orders of magnitude near the pair threshold $\varepsilon_{\perp} \sim 2$, and reduces to Erber's result in the limit $\varepsilon_{\perp} \gg 1$. It is a more accurate approximation than the very similar form obtained in Baring (1988). Eq. (27) incorporates domains where the created pairs are mildly-relativistic, and can be reliably applied in fields up to $B \sim 0.5$ when $\varepsilon_{\perp}B \gg 1$. Baier & Katkov (2007) also presented in their Eq. (B.5) polarization-dependent forms to account for near-threshold modifications to the polarized rate. Their results satisfied $\mathcal{F}_{\perp} \approx (\varepsilon_{\perp}^2 - 4)/(2\varepsilon_{\perp}^2) \mathcal{F}_{\parallel}$, from which one obtains

$$\mathcal{F}_{\perp}(\varepsilon_{\perp}, B) = \frac{\varepsilon_{\perp}^2 - 4}{\varepsilon_{\perp}^2 \sqrt{\mathcal{L}(\varepsilon_{\perp}) \phi(\varepsilon_{\perp})}} \exp\left\{-\frac{\phi(\varepsilon_{\perp})}{4B}\right\}, \quad (29)$$

and a partner form for \mathcal{F}_{\parallel} that can be applied even fairly close to its $\varepsilon_{\perp} = 2$ threshold. These results are used in our computations, though we observe that since Eq. (29) does not contain terms dependent on $1 + \sqrt{1 + 2B}$, it may not be precise near the pair threshold for \perp photons.

To provide an accurate treatment of the polarization dependence of pair thresholds, Story & Baring (2014) followed Harding, Baring & Gonther (1997) in adding a ‘‘patch’’ using the exact attenuation coefficients from Eq. (6) of Daugherty & Harding (1983) at sufficiently low energies, namely $\varepsilon_{\perp} < 1 + \sqrt{1 + 4B}$. We adopt an identical procedure here, for which photons with parallel and perpendicular polarization produce pairs only in the ground (0,0) and first excited (0,1) and (1,0) states respectively. Here (j, k) denotes the Landau level quantum numbers of the produced pairs. Thus, including only the (0,0) pair state for \parallel polarization gives

$$\mathcal{F}_{\parallel}^{\text{PP}} = \frac{2}{\varepsilon_{\perp}^2 |p_{00}|} \exp\left(-\frac{\varepsilon_{\perp}^2}{2B}\right), \quad \varepsilon_{\perp} \geq 2, \quad (30)$$

and only the sum of the (0,1) and (1,0) states for \perp polarization yields

$$\mathcal{F}_{\perp}^{\text{PP}} = \frac{2E_0(E_0 + E_1)}{\varepsilon_{\perp}^2 |p_{01}|} \exp\left(-\frac{\varepsilon_{\perp}^2}{2B}\right), \quad \varepsilon_{\perp} \geq 1 + \sqrt{1 + 2B}. \quad (31)$$

In these expressions, two energies of pairs appear:

$$E_0 = (1 + p_{01}^2)^{1/2}, \quad E_1 = (1 + p_{01}^2 + 2B)^{1/2},$$

where

$$|p_{jk}| = \left[\frac{\varepsilon_{\perp}^2}{4} - 1 - (j+k)B + \left(\frac{(j-k)B}{\varepsilon_{\perp}} \right)^2 \right]^{1/2},$$

describes the magnitude of the momentum parallel to \mathbf{B} . The pair production rate in this regime behaves like a wall at the thresholds given in Eqs. (30) and (31), and photons will create pairs as soon as they satisfy these kinematic restrictions. Note that we performed numerical tests that incorporated the next pair state threshold (p_{01}) for the \parallel polarization to add to the form Eq. (30), and found that the attenuation opacities were insensitive to this inclusion. Also, in the detailed analysis of pair opacities in pulsars and magnetars, Story & Baring (2014) observed that escape energies were not sensitive to the polarization character of this patch for pulsar fields, but that the polarization dependence of the threshold was influential for the supercritical field domain of magnetars, the main focus here. The importance of near-threshold treatment of pair opacity when $B > 1$ will become apparent in due course.

3 PHOTON SPLITTING ATTENUATION LENGTHS

In this section we compute the attenuation length for the photon splitting only. While escape energies are the prime focus of the paper, a brief presentation of attenuation lengths is motivated in validating the numerical determination of opacities. The reason why discussion of pair creation is omitted in this Section is that it is extensively documented in the works by Harding, Baring & Gonthier (1997), Baring & Harding (2001) and Story & Baring (2014). In particular, the analytic results herein for splitting attenuation of photons emitted above the stellar surface have not been developed elsewhere. In considering opacities for pair creation, Story & Baring (2014) developed an analytical approach to the integral of optical depth in Eq. (1) for photons initially emitted parallel to the field line near the magnetic axis, and for quasi-polar emission locales. Here we adopt a similar procedure and produce analogous analytic approximations for photon splitting. Flat Minkowski spacetime is presumed throughout this Section.

Using the propagation angle η as the integral variable instead of the pathlength s , the optical depth for photon splitting can be stated as

$$\tau_\sigma(l) = \frac{\alpha_f^3 \varepsilon^5}{60\pi^2 \lambda_c} \int_0^{\eta(l)} B^6 \mathcal{M}_\sigma^2 \sin^6 \Theta_{\text{kB}} \frac{ds}{d\eta} d\eta \quad . \quad (32)$$

Here the subscript σ denotes different splitting modes and the \mathcal{M}_σ is the corresponding amplitude coefficient, as defined in Eq. (21). For situations where the emitted photon population is unpolarized, the optical depth can be expressed as an average of the \perp and \parallel polarizations for the incident (attenuated) photon

$$\tau_{\text{ave}} = \frac{1}{2} (\tau_{\perp \rightarrow \parallel} + \tau_{\perp \rightarrow \perp\perp} + \tau_{\parallel \rightarrow \perp\perp}) \quad , \quad (33)$$

where the \perp state photons have two splitting channels.

The upper limit $\eta(l)$ is the inversion of Eq. (13) for path length $s = l$; in general, it is algebraically non-trivial. Note that since both the $\parallel \rightarrow \perp$ and $\parallel \rightarrow \parallel\perp$ orderings of the produced photons are incorporated in $\mathcal{R}_{\parallel \rightarrow \perp}^{\text{sp}}$ in Eq. (23), they are also included in $\tau_{\parallel \rightarrow \perp\perp}$ in Eq. (33), leading to $2\mathcal{M}_1^2$ contributions identifiable in Eq. (24), and Eq. (41) below.

Considering only the case of a photon emitted at small colatitude, $\theta_E \ll 1$, and the direction of the photon is exactly parallel to the local field line (i.e., $\Theta_e = 0$), η is well approximated by $l/(l + r_E)$. In this case, we also have

$$\delta_E \approx \frac{1}{2} \theta_E \quad , \quad (34)$$

as the emission angle relative to the local radial direction. Eq. (3) and Eq. (20) can be approximated as

$$B \approx B_p \frac{(\delta_E - \eta)^3}{h^3 \delta_E^3} \quad \text{and} \quad \sin \Theta_{\text{kB}} \approx \frac{3}{2} \eta \quad , \quad (35)$$

where $h = r_E/R_{\text{NS}}$ is the emission altitude scaled by the radius of the star. In addition, the Jacobian

$$\frac{ds}{d\eta} \approx \frac{r_E \delta_E}{(\delta_E - \eta)^2} \quad (36)$$

can be deduced with the help of the sine law adapted from Eq. (13). These results can be inserted into Eq. (32), yielding

an approximation for the optical depth. By changing the integration variable into $x = \eta/\delta_E$, and writing $x_{\text{max}} = l/(l + r_E)$, one arrives at

$$\tau_\sigma \approx \frac{243\alpha_f^3}{81920\pi^2} \frac{B_p^6 \varepsilon^5 \theta_E^6}{h^{17}} \frac{R_{\text{NS}}}{\lambda_c} \int_0^{x_{\text{max}}} \mathcal{M}_\sigma^2 (1-x)^{16} x^6 dx \quad . \quad (37)$$

Note that the magnetic field strength $B \approx B_p(1-x)^3/h^3$ is the argument of \mathcal{M}_σ and so appears inside the integral.

If one considers emission at different colatitudes but along a same field line, one has $\sin^2 \theta_E = h \sin^2 \theta_f$. Here θ_f is the footpoint colatitude, which is the colatitude of the field line when it intersects the surface of the star. In the small colatitude limit corresponding to polar locales, $\theta_E \approx \theta_f \sqrt{h}$. Then the optical depth integral assumes the form

$$\tau_\sigma \approx \frac{243\alpha_f^3}{81920\pi^2} \frac{B_p^6 \varepsilon^5 \theta_f^6}{h^{14}} \frac{R_{\text{NS}}}{\lambda_c} \int_0^{x_{\text{max}}} \mathcal{M}_\sigma^2 (1-x)^{16} x^6 dx \quad . \quad (38)$$

For small mean free paths for photon splitting, $l \ll hR_{\text{NS}}$, the upper limit $x_{\text{max}} \approx l/r_E$ of the integral is much less than unity. Then the magnetic field does not change much in both magnitude and direction along the path of the photon. Consequently, \mathcal{M}_σ can be approximated as the value at the emission point, i.e. $\mathcal{M}_\sigma \approx \mathcal{M}_\sigma(B_E)$, and be placed outside the integration. The magnitude of the field at the emission point is $B_E = B_p \sqrt{4 - 3h \sin^2 \theta_f} / (2h^3)$ and can be approximated by $B_E \approx B_p/h^3$ for quasi-polar locales. The leading order evaluation of the integral is then trivial, yielding

$$\tau_\sigma \approx \frac{243\alpha_f^3}{573440\pi^2} \frac{R_{\text{NS}}}{\lambda_c} \mathcal{M}_\sigma^2 B_p^6 \varepsilon^5 \theta_f^6 \left(\frac{l}{h^3 R_{\text{NS}}} \right)^7 \quad . \quad (39)$$

By setting $\tau_\sigma = 1$, the attenuation length $l \rightarrow L_\sigma$ is obtained as

$$L_\sigma \approx h^3 R_{\text{NS}} \left[\frac{573440\pi^2}{243\alpha_f^3} \frac{\lambda_c}{\mathcal{M}_\sigma^2 B_p^6 \theta_f^6 R_{\text{NS}}} \right]^{1/7} \varepsilon^{-5/7} \quad . \quad (40)$$

This is the analytic approximation for polar emission locales that serves as the photon splitting analog of the pair creation result in Eq. (30) in Story & Baring (2014). All modes possess attenuation lengths with energy dependence $\varepsilon^{-5/7}$, which applies at energies well below pair threshold. It is also a simple matter to sum the modes according to the prescription in Eq. (33) to generate the polarization-averaged attenuation length L_{ave} , which can be simply related to the conversion length for the $\perp \rightarrow \parallel$ mode in Eq. (40):

$$L_{\text{ave}} = \left[\frac{2\mathcal{M}_1^2}{3\mathcal{M}_1^2 + \mathcal{M}_2^2} \right]^{1/7} L_{\perp \rightarrow \parallel} \quad . \quad (41)$$

Note again that in all of Eqs. (39), (40) and (41), the emission point values $\mathcal{M}_\sigma \approx \mathcal{M}_\sigma(B_E)$ are assumed by the splitting amplitude coefficients.

The left panel of Fig. 2 illustrates how the attenuation lengths vary with photon energy for different polar magnetic fields and footpoint colatitudes, averaged over polarizations, i.e., using Eq. (33). The Figure is restricted to surface emission locales, so that $h = 1$ and $\theta_E = \theta_f$. The neutron star radius R_{NS} (marked) serves as the scale for curvature of field lines proximate to the surface, and separates the two main regions for the morphology of the attenuation length curves. For $L \ll R_{\text{NS}}$, the curves have a power-law behavior as $L \propto \varepsilon^{-5/7}$, which is inferred qualitatively in Harding,

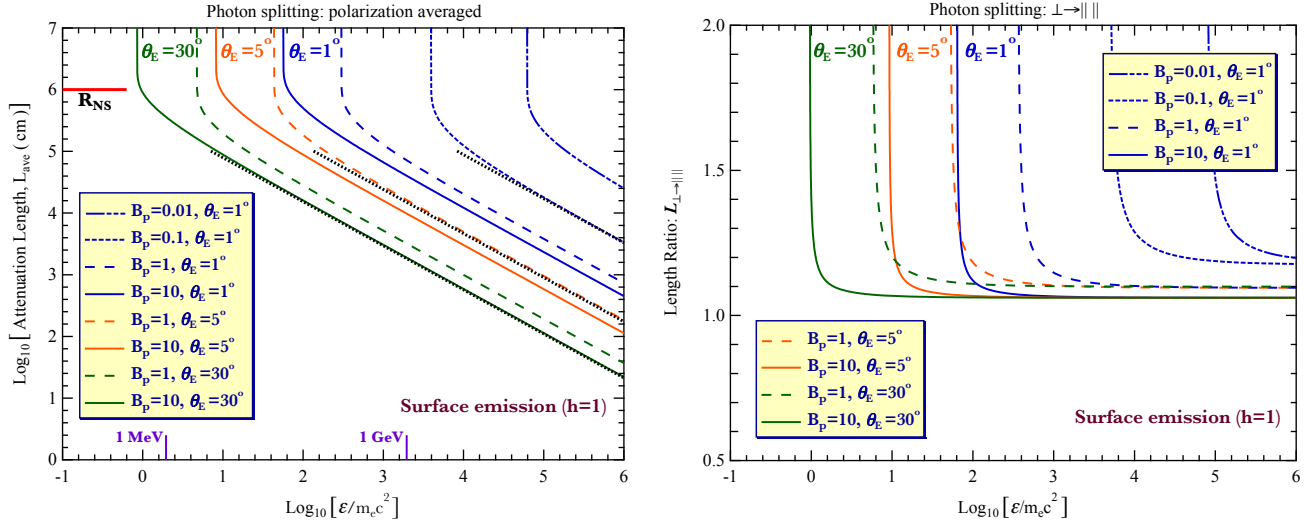


Figure 2. *Left Panel:* Attenuation lengths L_{ave} , averaged over all polarization modes for photon splitting, for light emitted from the neutron star surface ($h = 1$) and propagating in flat spacetime, initially parallel to the local field, plotted as a function of photon energy (in units of $m_e c^2$). Curves constitute numerical results obtained from Eq. (33), and are color-coded for emission colatitudes $\theta_E = 1^\circ$ (blue), $\theta_E = 5^\circ$ (orange) and $\theta_E = 30^\circ$ (green), as indicated. Different polar field strengths B_p are represented, labelled in units of B_{cr} . The dotted straight lines represent the analytic approximation from Eq. (41), for three cases: $B_p = 10$ and $\theta_E = 30^\circ$, $B_p = 1$ and $\theta_E = 5^\circ$, and $B_p = 0.1$ and $\theta_E = 1^\circ$. The solid red line on the upper left marks the neutron star radius R_{NS} , the pertinent scale for field line curvature near the surface. *Right Panel:* The ratio $L_{\perp \rightarrow \parallel} / L_{\text{ave}}$ of the attenuation length for the $\perp \rightarrow \parallel$ splitting mode from Eq. (32) to the average value L_{ave} derived from computation of Eq. (33). The sequence of θ_E and B_p values and associated color coding matches that on the left. See the text for a discussion of the two asymptotic domains at large ϵ and large $L_{\perp \rightarrow \parallel}$.

Baring & Gonthier (1997), and analytically here. Since the dipole magnetosphere is scale invariant in terms of its angular geometry, emission at higher altitudes reduces the local field according to $B_E \approx B_p/h^3$, and the emission colatitude scales as $\theta_E \approx \theta_f \sqrt{h}$. Thus, the simple approximate result $L_\sigma \propto h^3$ along a given field line emerges in Eq. (40), with some additional h dependence implicit in the \mathcal{M}_σ factors that is generally weak in subcritical fields that are encountered when $h \gtrsim 3 - 4$.

The attenuation length curves are declining functions of the photon energy. In the $L \gg R_{\text{NS}}$ domains, the attenuation lengths diverge and the vertical $L \rightarrow \infty$ asymptotes define the escape energies ϵ_{esc} , the subject of Section 4. Below these energies, the magnetosphere is transparent to photon splitting. The analytic approximation in Eq. (41) is also depicted as discrete dots, providing a precise match to the numerical results when $L \ll R_{\text{NS}}$. This analytic protocol also verifies the numerics of each of the splitting modes individually, but not illustrated graphically. The attenuation lengths decline with increasing B_p since the attenuation coefficients are increasing functions of the field strength. The attenuation lengths and escape energies decrease with θ_E , because at larger emission colatitudes, the radii of field line curvature are smaller, and photons require a shorter propagation distance in order to realize significant Θ_{KB} values.

The right panel of Fig. 2 shows the ratio $L_{\perp \rightarrow \parallel} / L_{\text{ave}}$ as functions of the photon energy ϵ and so serves as a proxy for $L_{\perp \rightarrow \parallel}$, whose curves would resemble those on the left panel. The vertical upturns in the curves at low energies illustrate that the escape energies for $\perp \rightarrow \parallel$ mode is generally greater than that of the polarization-averaged result, an obvious consequence of adding modes of opacity. The ratio curves become flat in the high energy domains since the opacities for all three modes scale as ϵ^{-5} .

Using Eq. (41), the asymptotic limits of the curves can be expressed as $L_{\perp \rightarrow \parallel} / L_{\text{ave}} = [(3\mathcal{M}_1^2 + \mathcal{M}_2^2) / 2\mathcal{M}_1^2]^{1/7}$, and the numerical results reproduce this analytic result well when ϵ is sufficiently high, i.e. a factor of ten or so above the escape energy. Monotonic declines of the length ratios and escape energies with emission colatitude θ_E and polar field strength B_p are obvious and expected.

It is often the case that the photons are not emitted exactly parallel to the local field. Relativistic electrons with finite Lorentz factors have a Doppler cone of emission due to aberration with a beaming angle $\Theta_e \sim 1/\gamma_e$. This applies to a wide variety of mechanisms, including curvature radiation, synchrotron and synchrotron self-Compton emission in gamma-ray pulsar models (e.g., Daugherty & Harding 1996; Romani 1996; Harding & Kalapotharakos 2015) and resonant inverse Compton scattering in scenarios for generating hard X-ray tail signals in magnetars (Baring & Harding 2007; Fernández & Thompson 2007; Beloborodov 2013; Wadiasingh et al. 2018). The development of an analytic approximation becomes rather simple if non-zero Θ_e is assumed. In this case, the opacity is achieved generally on scales much smaller than the radius of field line curvature, i.e. so that $L \ll hR_{\text{NS}}$. Accordingly, a uniform field can be assumed along the trajectory until $\tau = 1$ is realized, and the optical depth formula in Eq. (32) yields, to leading order in $L/(hR_{\text{NS}})$,

$$\tau_\sigma \approx \frac{\alpha_f^3}{60\pi^2} \mathcal{M}_\sigma^2 B_E^6 \epsilon^5 \sin^6 \Theta_e \frac{l}{\lambda_c} \quad (42)$$

Inverting this, the attenuation length is expressed as

$$L_\sigma \approx \frac{60\pi^2 \lambda_c}{\alpha_f^3} \mathcal{M}_\sigma^{-2} B_E^{-6} \epsilon^{-5} \sin^{-6} \Theta_e \quad (43)$$

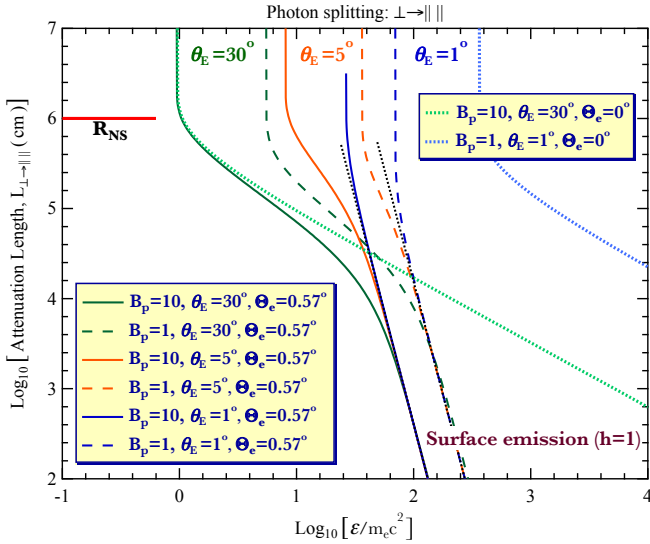


Figure 3. Flat spacetime attenuation lengths $L_{\perp \rightarrow \parallel}$ for the splitting mode $\perp \rightarrow \parallel$, as functions of photon energy (in units of $m_e c^2$). As in Fig. 2, the light is emitted from the neutron star surface. However, here most examples are for the light wavevector \mathbf{k} initially at a non-zero angle $\Theta_e \equiv \Theta_{\text{KB}} = 1$ radian to the local magnetic field vector \mathbf{B} . Different polar field strengths B_p are represented, labelled in units of B_{cr} . The dotted straight black lines represent the analytic approximation from Eq. (43), for two field choices $B_p = 10$ and $B_p = 1$, a result that is independent of the value of θ_E . The light green and blue dotted curves depict cases where $\theta_0 = 0$, i.e. light initially moving parallel to \mathbf{B} . The neutron star radius scale R_{NS} is marked at the upper left.

where again, \mathcal{M}_σ denotes $\mathcal{M}_\sigma(B_E)$. Numerical evaluations of the attenuation lengths for the $\perp \rightarrow \parallel$ mode attenuation lengths with a non-zero Θ_e are illustrated in Fig. 3. The $\Theta_e = 0$ cases and the analytic approximation from Eq. (43) are also plotted for comparison. The non-zero Θ_e cases exhibit a steep decrease in attenuation length in the high energy domain, with a $L \propto \varepsilon^{-5}$ dependence when $L \ll R_{\text{NS}}$, evinced in Eq. (43). For large footpoint colatitudes, $\theta_E \gtrsim 20^\circ$, a non-zero Θ_e does not change the escape energy much from $\Theta_e = 0$ values, a consequence of the comparatively short radius of curvature of field lines local to the emission point. However, when the footpoint colatitude is small, $\theta_E \lesssim 10^\circ$, the escape energy is strongly reduced, making it more difficult for high energy photons to escape.

4 ESCAPE ENERGIES FOR PHOTON SPLITTING AND PAIR CREATION

In this section the escape energies for both processes are explored. These energies form the prime focus of this paper, with a particular emphasis on their determination along field loops in the inner magnetosphere. This case more directly connects to magnetar emission models. The exposition starts with analytics in the small colatitude domain and then moves to illustrations of numerical results. The analytic derivations provide quantitative behavior of the escape energies that enhances the understanding of the numerics, and serves as checks on them. Flat Minkowski spacetime is assumed throughout.

4.1 Analytic Approximations: Small Colatitudes

For pair creation, an analytic approximation for escape energies in the small colatitude domain $\theta_f \ll 1$ was derived in Story & Baring (2014), using Erber’s asymptotic attenuation coefficient in Eq. (26). Since this is an exponential form that is sensitive to the photon propagation angle Θ_{KB} along the path, they used the method of steepest descents to evaluate the opacity integral, yielding

$$\varepsilon_{\text{esc}} = \frac{2^{13} h^{5/2}}{3^5 B_p \theta_f} \left\{ \log \left(\frac{3^6 \alpha_f R_{\text{NS}}}{2^{19} \lambda_c} \right) + \frac{1}{2} \log \left(\frac{3\pi \varepsilon_{\text{esc}} B_p^3 \theta_f^3}{2h^{11/2}} \right) \right\}. \quad (44)$$

This result assumes that the photons are emitted parallel to the local field, and that light propagates in straight lines. Since it is based on Erber’s approximation, it is applicable to subcritical fields and energies well above pair threshold. The second logarithmic term on the right hand side is only weakly dependent on its argument, so one can infer that $\varepsilon_{\text{esc}} \propto 1/B_p$ and $\varepsilon_{\text{esc}} \propto 1/\theta_f$, approximately. These couplings are direct consequences of the appearance of the product of $\varepsilon B \sin \Theta_{\text{KB}}$ in the argument of Erber’s exponential form, which generates the correlation $\varepsilon_{\text{esc}} B_p \theta_f \approx \text{constant}$ at quasi-polar colatitudes.

For photon splitting we modify the analytic approach employed by Story & Baring (2014) again treating the domain of small colatitudes. Eq. (38) serves as a natural starting point for photons emitted parallel to \mathbf{B} . For escape to an observer at infinity, we set $r \rightarrow \infty$, so that $x_{\text{max}} \rightarrow 1$, yielding the form

$$\tau_\sigma \approx \frac{3^5 \alpha_f^3}{2^{14} \cdot 5 \pi^2} \frac{R_{\text{NS}}}{\lambda_c} \frac{B_p^6 \varepsilon^5 \theta_f^6}{h^{14}} \mathcal{I}_\sigma, \quad (45)$$

for

$$\mathcal{I}_\sigma = \int_0^1 \mathcal{M}_\sigma^2 (1-x)^{16} x^6 dx. \quad (46)$$

Setting $\tau_\sigma = 1$, the escape energy is then expressed as

$$\varepsilon_{\text{esc}} \approx \left[\frac{2^{14} \cdot 5 \pi^2}{3^5 \alpha_f^3} \frac{\lambda_c}{R_{\text{NS}}} \frac{h^{14}}{B_p^6 \mathcal{I}_\sigma} \right]^{1/5} \theta_f^{-6/5}. \quad (47)$$

This is the analytic approximation for the photon splitting escape energy in the $\theta_f \ll 1$ domain that is analogous to Eq. (44), and is derived here for the first time. The energy dependence $\varepsilon_{\text{esc}} \propto \theta_f^{-6/5}$ emerges regardless of the surface field strength and it applies to all splitting modes. Note the argument of \mathcal{M}_σ is $B \approx B_p (1-x)^3 / h^3$, which comes from Eq. (35). Generally the integral in the denominator can only be solved numerically.

Observe that when $B_p/h^3 < 1$, $\mathcal{M}_\sigma(x)$ grows slowly with increasing x , as the field strength declines along an outward photon trajectory. Then \mathcal{M}_σ can be approximated by its value at the peak of the $(1-x)^{16} x^6$ profile, i.e. at $x = 3/11$, and can be placed outside the integration. Then Eq. (45) simplifies to

$$\tau_\sigma \approx \frac{\mu_p \alpha_f^3}{\pi^2} \frac{R_{\text{NS}}}{\lambda_c} \frac{B_p^6 \varepsilon^5 \theta_f^6}{h^{14}} \mathcal{M}_{\sigma,p}^2, \quad (48)$$

where

$$\mu_p = \frac{3^4}{2^{14} \cdot 2860165} \Rightarrow \frac{\mu_p \alpha_f^3}{\pi^2} \frac{R_{\text{NS}}}{\lambda_c} \approx 1.762 \quad (49)$$

for $R_{\text{NS}} = 10^6$ cm. Also,

$$\mathcal{M}_{\sigma,p} = \mathcal{M}_{\sigma} \left[B \left(x = \frac{3}{11} \right) \right] \approx \mathcal{M}_{\sigma} \left(\frac{512 B_p}{1331 h^3} \right) \quad (50)$$

is the value of \mathcal{M}_{σ} at $x = 3/11$. Setting Eq. (48) equal to unity, the escape energy can be expressed as

$$\varepsilon_{\text{esc}} \approx \left[\frac{\pi^2}{\mu_p \alpha_f^3} \frac{\lambda_c}{R_{\text{NS}}} \frac{h^{14}}{B_p^6 \mathcal{M}_{\sigma,p}^2} \right]^{1/5} \theta_f^{-6/5}, \quad (51)$$

or equivalently expressed in terms of the emission colatitude $\theta_E \approx \theta_f \sqrt{h}$:

$$\varepsilon_{\text{esc}} \approx \left[\frac{\pi^2}{\mu_p \alpha_f^3} \frac{\lambda_c}{R_{\text{NS}}} \frac{h^{17}}{B_p^6 \mathcal{M}_{\sigma,p}^2} \right]^{1/5} \theta_E^{-6/5}. \quad (52)$$

The asymptotic approximations in Eq. (51) and Eq. (52) have not been derived before in the literature, and obviously coincide for surface emission (i.e., $h = 1$). Both results apply for $\Theta_e = 0$ at the point of emission. We remark that they are most useful for locales where the emission point samples near-critical or subcritical fields. For highly supercritical values of B_p/h^3 , these two forms are less practical because the $(1-x)^3$ dependence of the \mathcal{M}_{σ}^2 factors shifts the peak of the \mathcal{I}_{σ} integral away from $x = 3/11$. In such circumstances, direct numerical evaluation of Eq. (47) is desirable, and is indeed the protocol adopted in the illustrations of Section 4.2.

The form in Eq. (52) needs to be adapted when h is not a constant parameter. Such is the situation where photons are emitted at various points along a specific field loop. The corresponding evaluation is then germane to the study of Wadiasingh et al. (2018) where the spectra of resonant inverse Compton scattering resulting from monoenergetic electrons moving along field loops is calculated. That work pertains to the persistent hard X-ray tails of magnetars, which will form part of the discussion in Section 4.3. The polar forms for these dipole field loops can be expressed as

$$\frac{r}{R_{\text{NS}}} = r_{\text{max}} \sin^2 \theta, \quad (53)$$

where r_{max} is the maximum (equatorial) radius of the loop rescaled by R_{NS} . These dipolar loops can also be parameterized by their footpoint colatitudes via $\sin \theta_f = 1/\sqrt{r_{\text{max}}}$, and the colatitude for a specific loop ranges from θ_f to $\pi - \theta_f$. The analytic approximation can be obtained by setting $h \approx r_{\text{max}} \sin^2 \theta_E \approx r_{\text{max}} \theta_E$ in Eq. (52):

$$\varepsilon_{\text{esc}} \approx \left[\frac{\pi^2}{\mu_p \alpha_f^3} \frac{\lambda_c}{R_{\text{NS}}} \frac{r_{\text{max}}^{17}}{B_p^6 \mathcal{M}_{\sigma,p}^2} \right]^{1/5} \theta_E^{28/5}. \quad (54)$$

Here

$$\mathcal{M}_{\sigma,p} \approx \mathcal{M}_{\sigma} \left(\frac{512}{1331} \frac{B_p}{\theta_E^6 r_{\text{max}}^3} \right), \quad (55)$$

and it needs to be evaluated at each colatitude θ_E along a loop. Eq. (54) is applicable to quasi-polar locales with small colatitudes $\theta_E \ll 1$, corresponding to a large value for r_{max} for a particular field loop. The strong dependence of the argument of the $\mathcal{M}_{\sigma,p}$ function on θ_E yields significant modifications to the $\theta_E^{28/5}$ dependence in supercritical fields near the stellar surface.

Analytic approximations for escape energies with a non-zero emission angle Θ_e are routinely derived in the meridional plane corresponding to $\zeta_E = 0$: see the right panel of

Fig. 1. The simplest path to the approximation is by replacing δ_E with $\delta_E + \Theta_e$. In the small colatitude domain where $\theta_E \ll \Theta_e$, Eq. (3) and Eq. (20) can be approximated as

$$B \approx B_p \frac{(\Theta_e - \eta)^3}{h^3 \Theta_e^3} \quad \text{and} \quad \sin \Theta_{\text{KB}} \approx \frac{3}{2} \eta - \Theta_e, \quad (56)$$

with the Jacobian

$$\frac{ds}{d\eta} \approx \frac{r_E \Theta_e}{(\Theta_e - \eta)^2}. \quad (57)$$

Again, these results can be inserted into Eq. (32), yielding an approximation for the optical depth

$$\tau \approx \frac{3^5 \alpha_f^3}{2^8 \cdot 5 \pi^2} \frac{B_p^6 \varepsilon^5 \Theta_e^6}{h^{17}} \frac{R_{\text{NS}}}{\lambda_c} \mathcal{J}_{\sigma} \quad (58)$$

with

$$\mathcal{J}_{\sigma} = \int_0^1 \mathcal{M}_{\sigma}^2 (1-x)^{16} \left(x - \frac{2}{3} \right)^6 dx. \quad (59)$$

Here the integration variable is $x = \eta/\Theta_e$, and the upper limit is $x_{\text{max}} \approx 1$. Setting $\tau(\infty) = 1$, one arrives at

$$\varepsilon_{\text{esc}} \approx \left[\frac{2^8 \cdot 5 \pi^2}{3^5 \alpha_f^3} \frac{\lambda_c}{R_{\text{NS}}} \frac{h^{17}}{B_p^6 \mathcal{J}_{\sigma}} \right]^{1/5} \Theta_e^{-6/5}. \quad (60)$$

One can numerically solve the integral and find the analytic approximation for the escape energy in the small Θ_e domain. When $B_p/h^3 < 1$, the same logic as for the evaluation of Eq. (47) applies and one can extract the \mathcal{M}_{σ} and evaluate the integral. This results in a form

$$\varepsilon_{\text{esc}} \approx \left[\frac{2196606720 \pi^2}{13^2 \cdot 8273 \alpha_f^3} \frac{\lambda_c}{R_{\text{NS}}} \frac{h^{17}}{B_p^6 \mathcal{M}_{\sigma,0}^2} \right]^{1/5} \Theta_e^{-6/5}. \quad (61)$$

Here the $\mathcal{M}_{\sigma,0}$ is evaluated at $x = 0$, which is the peak for the $(1-x)^{16} (x-2/3)^6$ profile. Accordingly, the argument of $\mathcal{M}_{\sigma,0}$ scales with B_p/h^3 and depends slightly on the colatitude θ_E of emission.

4.2 Numerical Results

The escape energies as functions of footpoint colatitude for the $\perp \rightarrow |||$ mode splitting are illustrated in the left panel of Fig. 4. The chosen polar field strengths B_p encompass much of the range of interest for both magnetars and highly-magnetized pulsars. Note that the field strength at the emission point is $B_f = B_p [\sqrt{1 + 3 \cos^2 \theta_f}]/2$. These results are for surface emission of outward-propagating photons only, and they are obtained from the $l \rightarrow \infty$ limit of Eq. (32), using a bisection decision algorithm to isolate the divergence of the attenuation length. The solid green curves represent the numerical results for the parallel emission cases, i.e. $\Theta_e = 0$, for $B_p = 0.1, 1, 10, 100$. The escape energies are declining functions of θ_f , realizing a power-law behavior $\varepsilon_{\text{esc}} \propto \theta_f^{-6/5}$ at small colatitudes that was first identified by Harding, Baring & Gonthier (1997). This power-law character is also obtained in the analytic approximation in Eq. (47), which is displayed as the dotted straight diagonal lines in the Figure. The excellent precision of the approximation is evident, and was obtained specifically for numerical determination of the I_1 integral. Note that only colatitudes up to the equator $\theta_f = 90^\circ$ are plotted, with cases of inward propagation into the optically (Thomson) thick surface layers in the other hemisphere being omitted.

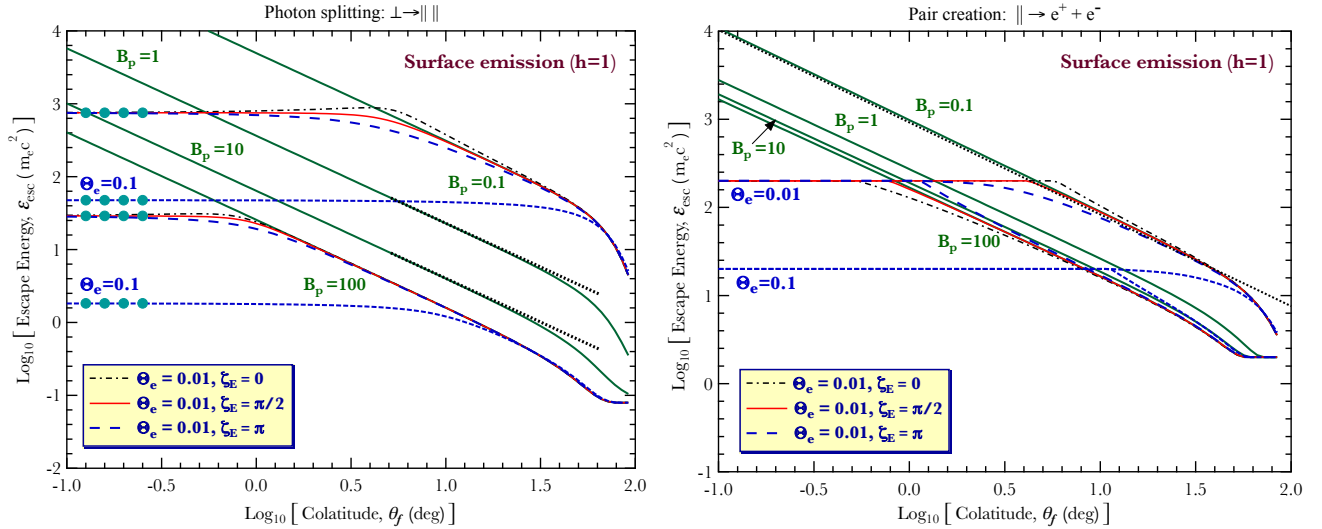


Figure 4. The escape energies ε_{esc} for photon splitting $\perp \rightarrow \parallel$ (left panel) and single photon pair production $\parallel \rightarrow e^{\pm}$ (right panel) for light emitted from the neutron star surface ($h = 1$) and propagating in flat spacetime. They are numerical results obtained by setting $L \rightarrow \infty$ in Eq. (2), and are plotted as functions of magnetic colatitude $\theta_E \equiv \theta_f$ for photon emission both along \mathbf{B} (solid green curves; $\Theta_e = 0$) and angles $\Theta_e = 0.1$ rad $\approx 5.7^\circ$ and 0.01 rad $\approx 0.57^\circ$ to the field (dashed blue, solid red and dash-dot black curves for $B_p = 0.1, 100$ cases only; see the legend). Consult Fig. 1 and Section 2.1 for the definition of the azimuthal angle ζ_E . The curves are grouped and labelled by their polar field strengths $B_p = 0.1, 1, 10, 100$. The escape energies for each process are monotonically decreasing functions of B_p for the range of parameters shown. The $\Theta_e = 0$ curves have slopes of $-6/5$ (splitting) and -1 (pair creation) at small θ_E , as identified by Harding, Baring & Gonthier (1997), and diverge near the polar axis, where the field line radius of curvature becomes infinite. The dotted black lines are the analytic approximations in Eq. (44) for pair creation and Eq. (47) for photon splitting. The filled aqua circles in the left panel denote evaluations using the analytic approximation in Eq. (60).

In the left panel of Fig. 4, non-zero Θ_e cases are also displayed for $B_p = 0.1$ and $B_p = 100$ as curves for different azimuth angle ζ_E . The most striking feature of these loci is that non-zero Θ_e reduces ε_{esc} substantially at small colatitudes, a property identified by Baring & Harding (2001) that is also evident in the attenuation length plot in Fig. 3. The origin of this ε_{esc} reduction is that magnetic field lines curve only slightly near the magnetic pole, so a non-zero value for Θ_e dramatically increases the $\perp \rightarrow \parallel$ attenuation coefficient due to its strong dependence on $\sin \Theta_{\text{kB}}$. The choices of $\Theta_e = 0.1$ and 0.01 correspond roughly to Lorentz cone angles for electrons of energies 5 and 50 MeV, respectively; these are appropriate for Compton upscattering models of magnetar hard X-ray emission (e.g. see Wadiasingh et al. 2018, and references therein). These curves coalesce with the $\Theta_e = 0$ examples when the emission colatitude exceeds Θ_e and field line curvature quickly establishes sufficiently large values for Θ_{kB} to govern the opacity phase space. Observe that the escape energy is generally insensitive to the value of ζ_E at both small and large emission colatitudes; this is no longer true when the emission angle Θ_e relative to \mathbf{B} exceeds about 10 degrees. When $\theta_f \ll \Theta_e$, the escape energies “plateau” at values independent of the choice of ζ_E . These values match those given by the analytic approximation in Eq. (60) that are depicted as filled aqua circles in the plot. Note that the morphology of escape energy curves for the other CP-permitted splitting modes is similar, albeit with slightly different values for ε_{esc} .

The right panel of Fig. 4 displays the escape energies as functions of surface colatitude for the $\parallel \rightarrow e^+ + e^-$ mode of pair creation, the polarization mode with the lowest pair threshold. Here the solid numerical curves are ob-

tained by the pair creation physics elements summarized in Section 2.2, specifically inserting Eq. (29) and Eq. (30) into Eq. (25). The $\Theta_e = 0$ curves display a power-law behavior as $\varepsilon_{\text{esc}} \propto \theta_f^{-1}$, which is slightly flatter than that for photon splitting, character first highlighted by Harding, Baring & Gonthier (1997). The analytic approximation in Eq. (44) is represented as the dotted straight diagonal line for the $B_p = 0.1$, noting that it becomes inaccurate at lower energies near threshold conditions. For low field cases like $B_p = 0.1$ or $B_p = 1$, the escape energies of pair creation are lower than those for photon splitting, thereby indicating the greater efficiency of the pair conversion process. In contrast, for $B_p = 10$ or $B_p = 100$, photon splitting escape energies drop significantly due to the strong dependence of the splitting rate on the field strength, and hence dominate pair creation opacity. This division of the competitiveness of the two processes based on field strength was highlighted in the study by Baring & Harding (1998). Non-zero Θ_e cases are also depicted for pair creation. It is noticeable that curves with the same Θ_e but different B_p merge in the small colatitude plateau domain, $\theta_f \ll \Theta_e$, because pair conversion $\gamma \rightarrow e^+e^-$ is very effective and photons will produce pairs as soon as they satisfy the kinematic threshold restriction in Eq. (30) during their propagation through the magnetosphere. Accordingly, the asymptotic values in the $\theta_f \ll \Theta_e$ regime only depend on Θ_e via the threshold criterion $\varepsilon_{\text{esc}} = 2/\sin \Theta_e$. A horizontal tail appears in the equatorial regime on the right hand side of the Figure. This tail marks the absolute threshold $\varepsilon_{\text{esc}} = 2$ for pair creation, realized because Θ_{kB} approaches $\pi/2$ rapidly during photon passage through the magnetosphere.

It is noteworthy that the general properties of the escape energy curves in both panels of Fig. 4 reproduce

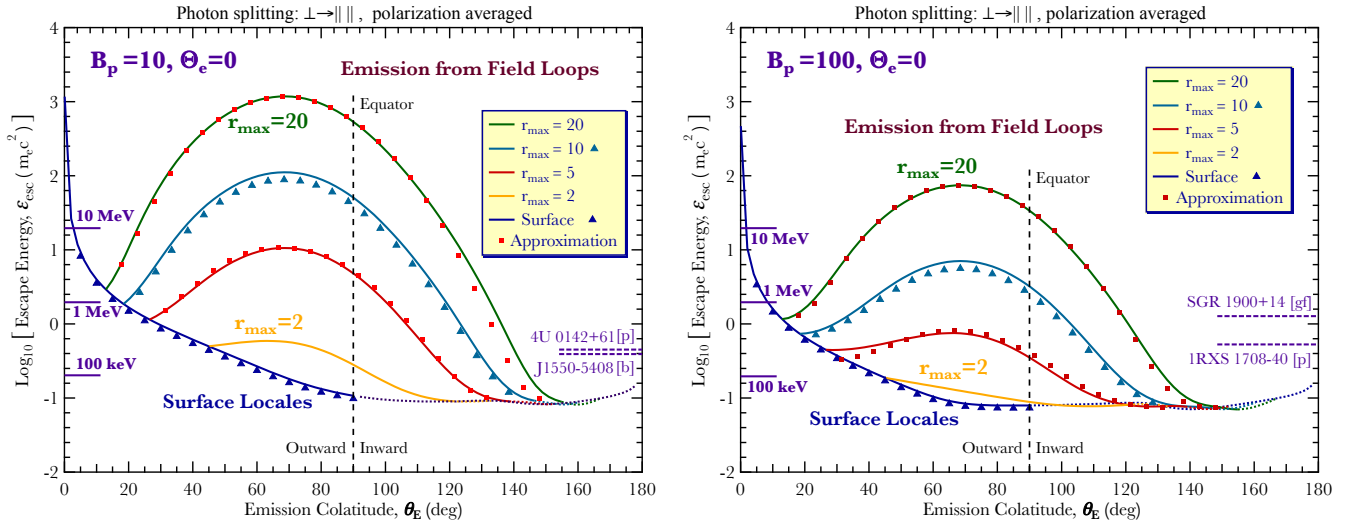


Figure 5. Photon splitting escape energies in flat spacetime for the mode $\perp \rightarrow \parallel$ (curves) and also averaged over polarization modes (triangles), for emission initially parallel to the local magnetic field line ($\Theta_e = 0$). The left and right panels are for surface polar fields $B_p = 10$ and $B_p = 100$, respectively. The abscissa is the emission colatitude θ_E , spanning outward propagation cases to the left of the equatorial marker line, to inward propagation to the right of this vertical dashed line. Four of the $\perp \rightarrow \parallel$ curves are for magnetospheric emission at points along dipolar magnetic field loops, labelled by $r_{\max} = 2, 5, 10, 20$, the maximum loop altitude in units of R_{NS} . In contrast, the dark blue curves for both panels are not for loop emission, but are surface emission cases that are displayed in the left hand panel of Fig. 4. All curves include dotted portions in the inward trajectory hemisphere that demarcate cases where photons would impact the stellar surface if not attenuated beforehand; these are generally near $\theta_E \sim 180^\circ$ for magnetospheric loop examples. In addition, escape energies for polarization-averaged opacities are exhibited as triangles for the surface emission and $r_{\max} = 10$ cases only. At the lower right of each panel are marker energies (purple dashed lines) signifying the approximate maximum energy observed in several magnetars with polar fields somewhat close to the illustrated values, SGR J1550-5408 (bursts, [b]), AXPs 4U 0142+61 and 1RXS 1708-40 (persistent emission, [p]), and SGR 1900+14 (giant flare, [gf]); see text for details.

those exhibited in Fig. 1 of Baring & Harding (2001) for $0.1 \leq B_p \leq 3.16$, though the values of ε_{esc} were lower by about factors of 1.3–1.8 therein because of their treatment of general relativistic effects for propagation from the surface. The focus on flat spacetime results here is adopted to facilitate comparison with compact analytic approximations.

4.2.1 Emission Along Magnetic Field Loops

A key aspect of the magnetar opacity problem that has not been discussed before in the literature concerns emission along field lines at low altitudes, an element that connects directly to models for their magnetospheric emission. Emission persists for many dynamical (light crossing) times, even in transient flare activity, so plasma trapping by closed field lines is naturally presumed. Therefore, an investigation of opacity in closed field regions above the stellar surface is motivated. One anticipates that general relativistic influences are likely to have limited impact on the escape energies at altitudes $r \gtrsim 2R_{\text{NS}}$, an element that is addressed in Sec. 5.

Fig. 5 illustrates the photon splitting escape energies ε_{esc} as functions of emission colatitude θ_E for photons emitted along specific magnetic field loops, i.e. $\Theta_e = 0$. The surface polar field strengths chosen, $B_p = 10$ or $B_p = 100$, are clearly appropriate for magnetars, and suggest a monotonic decline of escape energies with increasing B_p . Extrapolating to lower field values would lead to corresponding increases in the values of ε_{esc} . The bell-shaped curves represent the escape energies for $\perp \rightarrow \parallel$ mode splitting corresponds to field loops labelled by $r_{\max} = 2, 5, 10, 20$, color-coded as in the legend. The solid blue curves display the ε_{esc} for surface emission, and are identical to the corresponding curves in the

left panel of Fig. 4, though extended here to $\theta_f > 90^\circ$ colatitudes via the dotted portions. As with Fig. 4, the magnetosphere is opaque to photons with energies exceeding ε_{esc} and transparent to those with energies below this value.

Loop emission curves begin and end on the surface emission curve at the two footpoint colatitudes. Each of these loop emission curves exhibits a peak at around $\theta_E \sim 70^\circ$, either side of which ε_{esc} decreases sharply. To aid identification of the magnetic hemispheres, the vertical dashed lines represent the colatitude for equator, dividing the regions where photons are emitted outward and inward. The escape energy curves are asymmetric about the equator mostly because of inherent differences in field strengths and Θ_{KB} values for outward and inward trajectories. The dotted parts of the inward portions of all curves (at the largest colatitudes) denote the shadowing cases in which emitted photons would impact the stellar surface; in such circumstances, whether photon splitting happens or not is largely irrelevant. Observe that near the lower polar regions $\theta_E \sim 180^\circ$, there is some slightly non-monotonic behaviour for the curves, originating in the complex interplay between field magnitudes and field line curvature in determining splitting attenuation lengths. Escape energies for polarization-averaged emission are also depicted as triangles for surface emission and loop emission with $r_{\max} = 10$. These “loci” are at slightly lower ε_{esc} than the $\perp \rightarrow \parallel$ case, since $\mathcal{R}_{\text{ave}}^{\text{sp}}$ is always greater than $\mathcal{R}_{\perp \rightarrow \parallel}^{\text{sp}}$. Finally the red squares in the Figure represent an empirical approximation for loop emission, which is generally applicable for moderate altitudes. This is detailed in the Appendix, with the red dots representing computations us-

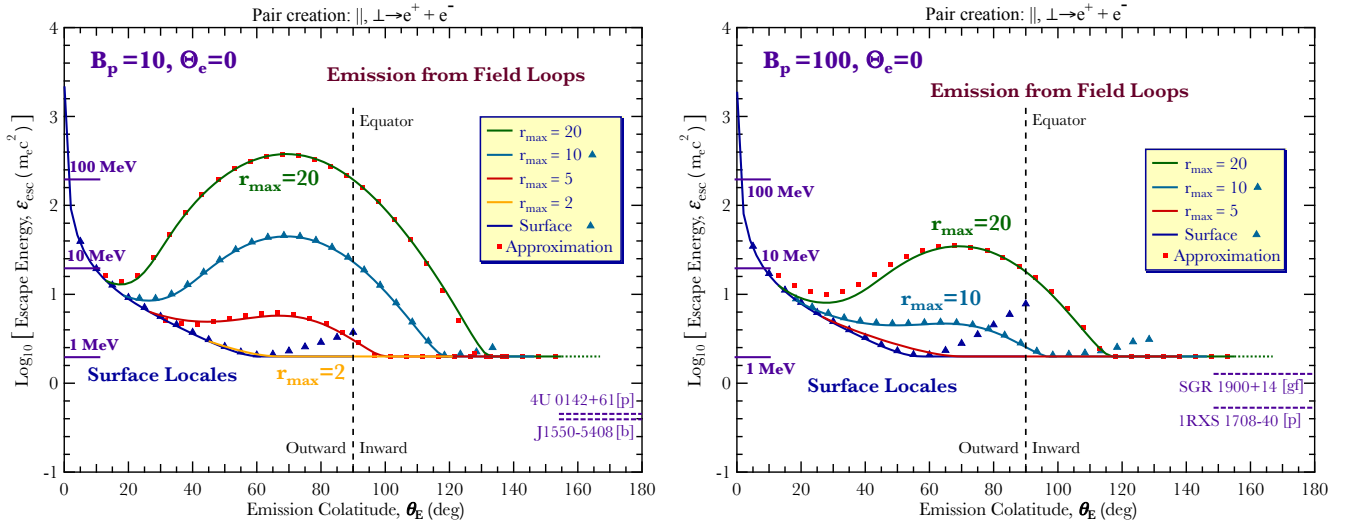


Figure 6. Pair creation escape energies in flat spacetime as functions of emission colatitude θ_E , for the polarization modes $\parallel \rightarrow e^+e^-$ (curves) and $\perp \rightarrow e^+e^-$ (triangles), for the meridional case of light propagation initially parallel to the local magnetic field line ($\Theta_e = 0$). The left and right panels are for surface polar fields $B_p = 10$ and $B_p = 100$, respectively. The r_{max} choices and other details are as for Fig. 5. The dark blue curves for both panels are again for surface emission cases that are displayed in the right panel of Fig. 4. The escape energies for $\perp \rightarrow e^+e^-$ opacities, exhibited as triangles for the surface emission and $r_{\text{max}} = 10$ cases only, are higher than those for $\parallel \rightarrow e^+e^-$ because of the higher threshold and lower conversion rate. Note that the purple dashed lines defining marker maximum observed energies of various magnetars (see Fig. 5) are lower than the absolute threshold of pair creation, $2m_e c^2$.

ing Eq. (76), and is useful for implementation in magnetar emission models: see Sec. 4.3.

Fig. 5 also includes markers signifying the approximate maximum energies detected for four different magnetars, sampling both quiescent and flaring emission. These serve as lower bounds to implied turnover energies, and provide a benchmark for interpreting how photon splitting can impact the spectrum emergent from the magnetosphere. The magnetars were selected so that their polar field values, as inferred from pulsation timing, were relatively proximate to the $B_p = 10, 100$ choices in the respective panels. The timing ephemerides enable estimates of $B_p \sin \alpha \sim 6.4 \times 10^{19} \sqrt{P\dot{P}}$ in the vacuum rotator case (Shapiro & Teukolsky 1983), serving as lower bounds to B_p . Here α is the inclination angle between the stellar rotation and magnetic moment axes. The inferred field strengths are also impacted by plasma loading of the magnetosphere, where currents contribute as well as Poynting flux in transporting angular momentum to infinity (e.g., see Harding, Contopoulos & Kazanas 1999). For various magnetars, equatorial field values $B_p/2$ for the case of orthogonal rotators ($\alpha = 90^\circ$) are listed in the McGill magnetar catalog (Olausen & Kaspi 2014). The maximum energies for the persistent emission data in pulsed hard X-ray tails are 230 keV for AXP 4U 0142+61 (den Hartog et al. 2008a), which has $B_p = 2.7 \times 10^{14}$ G, and 270 keV for AXP 1RXS 1708-40 (den Hartog et al. 2008b) with $B_p = 9.3 \times 10^{14}$ G, both sources being observed by INTEGRAL. The representative maximum energies for flaring activity are 200 keV for SGR J1550-5408 ($B_p = 4.3 \times 10^{14}$ G) during its storm of bursts dating from January 2009 (see van der Horst et al. 2012, for *Fermi*-GBM observations), and 650 keV for SGR 1900+14 ($B_p = 1.4 \times 10^{15}$ G) during its sole detected giant flare on 27 August 1998 (see Feroci et al. 1999, for *BeppoSAX* data).

Comparison between the escape energy contours and these observational results constrains the probable magnetospheric location of hard X-ray emission in the selected magnetars — similar inferences can be made for other such ultra-magnetized neutron stars. For $B_p = 10$ cases, the observed maximum energy for persistent emission from 4U 0142+61 is comparable to the peak value of the $r_{\text{max}} = 2$ curve. Thus the \perp polarization state photons cannot be emitted from the region with $r_{\text{max}} < 2$, otherwise the maximum observed energy would be attenuated by photon splitting. For the $r_{\text{max}} = 5$ loop, the escape energy curve exceeds the maximum observed energy for $\theta_E < 115^\circ$. Therefore, for loop emission with $r_{\text{max}} = 5$ colatitudes greater than 115° are forbidden by the 4U 0142+61 observations as described in den Hartog et al. (2008a); these correspond to inward propagation at emission points. Similarly, for $B_p = 100$ cases, magnetospheric regions with $r_{\text{max}} \lesssim 4$ are completely forbidden by the maximum observed energy for the persistent emission of 1RXS 1708-40, while the $r_{\text{max}} = 5$ loop is permitted at low colatitudes ($\theta_E < 85^\circ$). The reason for this θ_E asymmetry is that the inward emission at high colatitudes precipitates propagation into regions with strong fields and shorter radii of field curvature, so that consequently the escape energies decline. Polarization-averaged conclusions about permitted emission locales are similar, i.e. one would make similar inferences for the locales of origin of \parallel photons if they are allowed to split. Polar colatitudes, corresponding to very large r_{max} , are generally transparent to photon splitting, because the field line curvature is small, and photons generally propagate almost parallel to \mathbf{B} for long distances. This property can be deduced from Eq. (54).

Fig. 6 is the pair creation analog of the photon splitting results in Fig. 5. Solid curves here represent the escape energies for $\parallel \rightarrow e^+e^-$ mode pair creation for both loop emission and surface emission. The $r_{\text{max}} = 2$ curve is omitted in the

$B_p = 100$ panel because it overlaps the surface emission curve, being essentially visually indistinguishable. In contrast to the photon splitting plots, the pair creation escape energy curves here decrease slightly at first with increasing emission colatitude, then increase for the cases with large r_{\max} . For the $r_{\max} = 20$ case in the left panel in Fig. 6, the escape energy curve declines from the footpoint colatitude to around 17° . This is because the attenuation coefficient rate only weakly depends on the field strength in the supercritical field region (see Fig. 4). The escape energy curves are then determined primarily by the curvature of the dipolar field, and approach the surface emission curves for small r_{\max} cases. Such character was identified by Story & Barling (2014). As θ_E continues to increase, then the drop in B_E with altitude impacts the opacity as the field becomes sub-critical, and ε_{esc} then rises and eventually peaks before beginning to fall as the equator is approached. Eventually at large emission colatitudes θ_E , all the escape energy curves realize the horizontal plateau corresponding to the absolute pair threshold $2m_e c^2$. This is because photons quickly satisfy the pair threshold criterion $\varepsilon_{\text{esc}} \sin \Theta_{\text{KB}} > 2$ for inward propagation into stronger, converging fields.

Escape energies for $\perp \rightarrow e^+e^-$ mode creation are displayed as triangles for surface emission and loop emission with $r_{\max} = 10$. Their behavior imitates the corresponding $\parallel \rightarrow e^+e^-$ curves at first, but then they rise near the colatitudes where the $\parallel \rightarrow e^+e^-$ curves realize the threshold tails, since the threshold for $\perp \rightarrow e^+e^-$ is not constant, but an increasing function of field strength — see Eq. (31). Analogous to Fig. 5, the red squares in the figure represent an empirical approximation for pair creation, detailed in the Appendix — see Eq. (77). This approximation is fine for most loop colatitudes, but is not very accurate for low altitude cases where the escape energy curves decrease with increasing emission colatitude. Notwithstanding, both this empirical form, and that for photon splitting, provide tools useful for assessing the importance of attenuation in emission models for magnetars, an element that will be addressed in Sec. 4.3.

Identical to Fig. 5, the maximum observed energies ε_{\max} from typical magnetars are also marked in the bottom right of each panel, again serving to define lower bounds to ε_{esc} . As these energies are lower than the absolute threshold of pair creation, it is obvious that pair creation opacity cannot be responsible for attenuating photons at or below the maximum energies observed in either persistent or flaring magnetar emission. Yet, being generally below around 10–20 MeV when $r_{\max} \leq 10$, the ε_{\max} do provide important constraints that may explain why *Fermi*-LAT has not detected persistent emission from magnetars above 100 MeV (Abdo et al. 2010; Li et al. 2017). In comparing these pair creation results with escape energies for photon splitting, it is evident that the peak ε_{esc} value of each bell-shaped curve here is often lower than that of their photon splitting counterparts in Fig. 5. This is because the field strength drops rapidly with the increase of the colatitude for those emission loops possessing $r_{\max} > 5$. So if we combine both photon splitting and pair creation, the escape energy curves for loop emission should be dominated by pair creation for quasi-equatorial regions near the peak escape energy and the “wings” of the curves near the field line footpoint colatitudes are dominated by photon splitting. This generic division ap-

plies to both $B_p = 10$ and 100 cases; the combined opacity is presented in Fig. 10 in Sec. 5.

Non-zero emission angles Θ_e are required by most magnetar flare models, wherein the hard X-ray signals are produced by hot magnetospheric pair plasma. Fig. 7 illustrates the escape energies ε_{esc} as functions of emission colatitude for the $r_{\max} = 5$ loop with mostly non-zero emission angle Θ_e , for $\perp \rightarrow \parallel \parallel$ mode photon splitting and $\parallel \rightarrow e^+e^-$ mode pair creation. The $\Theta_e = 0$ and surface emission cases are also depicted for comparison. For each Θ_e value, two azimuth angle ($\zeta_E = 0, 180^\circ$) cases are plotted. Curves with other azimuth angles lie between these two curves and are not depicted here to enhance clarity of the Figure. For the $\perp \rightarrow \parallel \parallel$ mode photon splitting (left panel), a non-zero Θ_e will generally lower the escape energy curves and tends to shift the peaks to higher colatitudes ($\zeta_E = 180^\circ$ cases) or lower colatitudes ($\zeta_E = 0$ cases). For some $\zeta_E = 0$ cases, a second peak appears at a high colatitude. For photons emitted with $\zeta_E = 0$ propagating inward, the increase of the field strength and the field line curvature strongly reduces the escape energy at quasi-equatorial colatitudes, thus creating the valley and the second peak for the curve. This feature is evident in the $\Theta_e = 90^\circ$, $\zeta_E = 0$ curve, which realizes a symmetric double peak shape with respect to the equator because of the symmetry of the dipole field; a similar symmetry is possessed by the $\Theta_e = 90^\circ$, $\zeta_E = 180^\circ$ curve. The quasi-equatorial points for the $\Theta_e = 90^\circ$, $\zeta_E = 0$ curve are omitted, generating gaps in the curve corresponding to photon trajectories that impact the star surface. For the inward region of the Figure ($\theta_E > \pi/2$), a non-zero Θ_e , $\zeta_E > 90^\circ$ emission direction actually increases the escape energy above the $\Theta_e = 0$ values, since the photon trajectory is then directed away from the polar region where the field strength is very strong. Clearly $\zeta_e = 0$ cases have increased colatitude domains that are excluded as emission zones for the highest energy photons observed from 4U 0142+61 (persistent signal) and SGR J1550-5408 (bursts).

The $\parallel \rightarrow e^+e^-$ mode escape energies are illustrated in the right panel of Fig. 7. The general behavior of the escape energy curves resembles that of their $\perp \rightarrow \parallel \parallel$ counterparts. Curves with a large $\Theta_e = 30^\circ, 90^\circ$ realize plateaux when $\theta_E \lesssim 50^\circ$. This is because these small colatitudes correspond to relatively low altitude and strong field strength, so that pair conversion is very efficient and a photon will create pairs as soon as it satisfies the threshold criteria. Then a non-zero Θ_e establishes an effective threshold of $\varepsilon_{\text{esc}} = 2/\sin \Theta_e$, and photons with higher energies will be attenuated once emitted. This upper bound is clear for the $\Theta_e = 30, 90$ cases, but not for the $\Theta_e = 10$ cases since their entire escape energy curves are below that bound. This upper bound is broken at large colatitude regions, around $\theta_E \sim 68^\circ$ for $r_{\max} = 5$, because of the reduction of the field strength. Then the bell shape appears. For the $\Theta_e = 90^\circ$ cases, the upper bound coincides with the $2m_e c^2$ absolute threshold, thus at most colatitudes the escape energy curves are horizontal lines. In addition, for the $\Theta_e = 90^\circ$, $\zeta_E = 0$ case, the escape energy curve is slightly distorted near the absolute threshold. This is because the pair creation coefficients $\mathcal{R}_{\parallel, \perp}^{\text{pp}}$ are not monotonically-increasing functions of photon energy when occupation of only the first or ground Landau levels is possible: see Eqs. (30) and (31) for details.

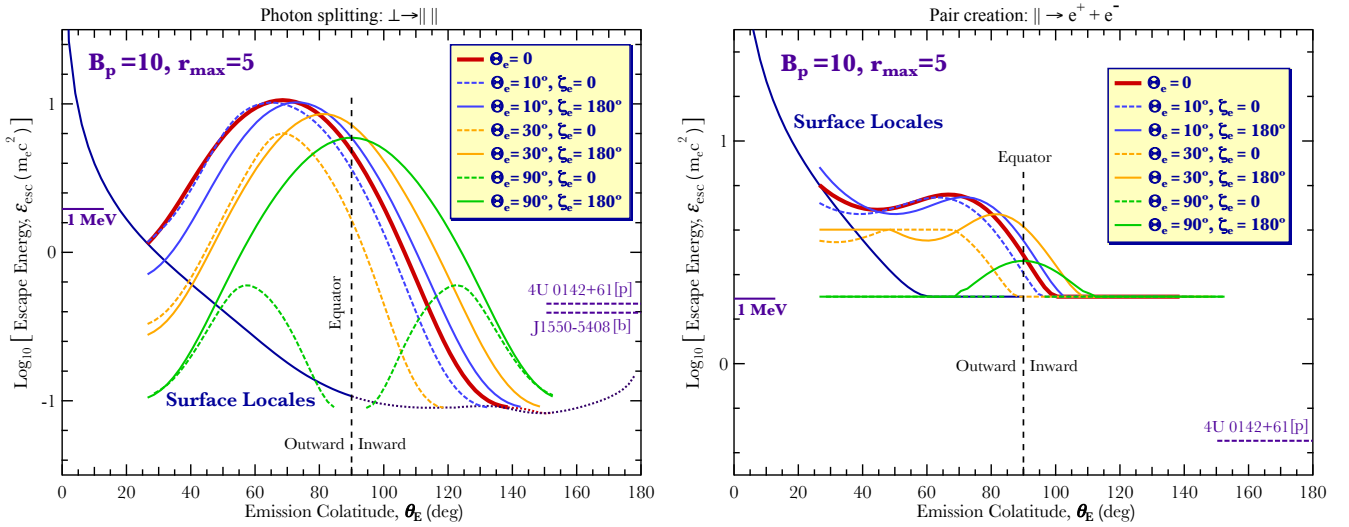


Figure 7. The escape energies ε_{esc} for photon splitting $\perp \rightarrow \parallel$ (left panel) and single photon pair production $\parallel \rightarrow e^+e^-$ (right panel) as functions of emission colatitude θ_E , for magnetospheric emission at points along the dipolar magnetic field loop with $r_{\text{max}} = 5$ and $B_p = 10$, propagating in flat spacetime. Curves are color-coded for initial emission angle $\Theta_e = 0$ (dark red, heavyweight), $\Theta_e = 10^\circ$ (blue), $\Theta_e = 30^\circ$ (orange) and $\Theta_e = 90^\circ$ (green). The $\Theta_e = 0$ cases are those displayed in the left panel of Fig. 5 and Fig. 6, respectively. Different azimuth angles ζ_E (see section 2.1) are represented by different line styles: dashed curves for $\zeta_E = 0^\circ$ and solid curves for $\zeta_E = 180^\circ$. The dark blue curves in each panel are for surface emission cases that are displayed in Figs. 4, 5 and 6.

4.3 Photon Splitting Opacity and Resonant Compton Upscattering in Magnetars

To forge a more direct connection between the opacity determinations and magnetar observations, it is insightful to consider a specific emission model. An appropriate choice is the resonant inverse Compton scattering scenario, which is regarded to be the dominant mechanism (Baring & Harding 2007; Fernández & Thompson 2007; Baring, Wadiasingh & Gonthier 2011; Nobili et al. 2008; Beloborodov 2013; Wadiasingh et al. 2018) for the generation of persistent hard X-ray emission. As noted in the Introduction, such resonant Compton scattering of soft thermal X-rays from magnetar surface layers or atmospheres by relativistic electrons/positrons in activated regions of their magnetospheres is extremely efficient due to the predominance of scatterings in the fundamental cyclotron resonance, i.e. at $\varepsilon = B$ in the electron rest frame. In that model, since $(\boldsymbol{\Omega} \times \mathbf{r}) \times \mathbf{B}$ drift velocities are small in the inner magnetospheres of slowly-rotating magnetars, the relativistic e^\pm of dimensionless momenta $\mathbf{p}_e = \gamma_e \boldsymbol{\beta}_e$ move along magnetic field lines, i.e. $\mathbf{p}_e \cdot \mathbf{B}_E / (|\mathbf{p}_e| |\mathbf{B}_E|) = \pm 1$. This is because transverse energies of these pairs are radiated away extremely efficiently, with cyclotron cooling timescales much shorter than 10^{-16} seconds. The interacting leptons thus can be safely assumed to occupy their ground state Landau level in a quantum description. Note that throughout this discussion, \mathbf{B}_E denotes the magnetic field vector at the point of scattering.

The impact of photon splitting and pair creation in attenuating such emission is obviously greatest for the highest energies. The approximate maximum photon energy in this upscattering mechanism differs from traditional invocations of inverse Compton scattering due to the kinematics of the process. The kinematics for resonant Compton scattering (e.g., Daugherty & Harding 1986) does not match that for field-free Compton scattering, since momentum transverse to an external field does not have to be conserved in QED.

Yet, energy conservation still holds in the presence of the magnetic field, and the upscattered photon energy is ultimately bounded by $\gamma_e m_e c^2$. For incident soft photon energies $m_e c^2 \varepsilon_s \sim kT \sim 0.5$ keV emanating from magnetar surface layers, the scattering generally leaves the electron in its ground Landau state (Gonthier et al. 2000, 2014). Moreover, owing to relativistic aberration when $\gamma_e \gg 1$, the incident photon is essentially parallel to \mathbf{B} in the electron/positron rest frame. Under these assumptions, and restricting the discussion to Minkowski spacetimes, the maximum resonant scattered photon energy in the observer frame is (Baring & Harding 2007; Baring, Wadiasingh & Gonthier 2011; Wadiasingh et al. 2018)

$$\varepsilon_f^{\text{max}} = \gamma_e (1 + \beta_e) \left[\frac{B_E}{1 + 2B_E} \right], \quad B_E = |\mathbf{B}_E|. \quad (62)$$

The maximum outgoing photon momentum \mathbf{k}_f ($\equiv \mathbf{k}$) is directed parallel to the lepton momentum at the interaction point $\mathbf{p}_e \cdot \mathbf{k}_f / (|\mathbf{p}_e| |\mathbf{k}_f|) = 1$, i.e., $\Theta_e \approx 0$ in the notation of Section 4.1. Eq. (62) dictates the effective cut-off for the inverse Compton upscattered spectrum, for any instantaneous viewing angle with respect to the magnetic axis $\hat{\boldsymbol{\mu}}$. An exception to this occasionally arises when the scattering samples soft photons deep in the Wien tail of the quasi-Planck spectrum radiating from the stellar surface, and the emission is exponentially suppressed. There is also some low-level, non-resonant emission appearing a little above $\varepsilon_f^{\text{max}}$.

Specializing to the dipole field adopted throughout this paper, one may specify B_E in terms of magnetic colatitude θ_E via $B_E = B_p R_{\text{NS}}^3 \sqrt{1 + 3 \cos^2 \theta_E} / (2r^3)$, where $r/R_{\text{NS}} = r_{\text{max}} \sin^2 \theta_E$ using a loop's altitude parameter r_{max} . If $\hat{\mathbf{n}}_v$ is the unit vector signifying the direction to an observer (i.e., $\hat{\mathbf{n}}_v = \mathbf{k}_f / |\mathbf{k}_f|$), in uniformly-activated magnetospheres, only specific colatitudes at meridional and antimeridional field loops locales satisfy the alignment con-

dition

$$\frac{\mathbf{p}_e \cdot \hat{\mathbf{n}}_v}{|\mathbf{p}_e|} = 1 \quad , \quad (63)$$

which is required for Eq. (62) to be operable. Accordingly, the conditions for strong Doppler-boosted and collimated upscattering emission are readily identifiable geometrically. The meridional/antimeridional plane is that defined by the two vectors $\hat{\boldsymbol{\mu}}$ and $\hat{\mathbf{n}}_v$, and therefore rotates with the star as it spins and $\hat{\boldsymbol{\mu}}$ traces out a conical surface. For leptons moving along field lines from the southern to the northern magnetic footpoints, the colatitude θ_E of interaction points satisfying Eq. (63) is found in Eq. (34) of Wadiasingh et al. (2018), wherein θ_0 corresponds to θ_E here:

$$\cos \theta_E \approx \pm \sqrt{[2 + \cos^2 \theta_v - \cos \theta_v \sqrt{8 + \cos^2 \theta_v}] / 6} \quad . \quad (64)$$

The dot product $\hat{\boldsymbol{\mu}} \cdot \hat{\mathbf{n}}_v = \cos \theta_v$ captures information on the instantaneous viewing angle θ_v to the magnetic axis. The two branches of this relation correspond to antimeridional (+) and meridional (−) loops, respectively, when *the leptons traverse from south to north*. These two branches demarcate two hemispheres: antimeridional loops sample $0 < \theta_E < \pi/2$, while meridional ones correspond to $\pi/2 < \theta_E < \pi$. Thus, for an observer staring down towards the north pole, the emission points for the meridional loop are in the southern hemisphere, and in the northern hemisphere for the antimeridional loop. The range of allowed colatitudes for a field line above the stellar surface is bounded by its footprint colatitudes: $\theta_{\min} < \theta_E < \theta_{\max}$ where $\theta_{\min} = \arcsin \sqrt{1/r_{\max}}$ and $\theta_{\max} = \pi - \theta_{\min}$. When the leptons move in the opposite direction along the loops, from north to south, the hemispheres comprising the meridional and antimeridional loops are interchanged, as are the applicable signs for the approximate identity in Eq. (64).

If pulsating magnetars are inclined rotators, with an angle α between the spin ($\hat{\boldsymbol{\Omega}}$) and magnetic ($\hat{\boldsymbol{\mu}}$) axes that satisfies $\cos \alpha = \hat{\boldsymbol{\Omega}} \cdot \hat{\boldsymbol{\mu}}$, then as the star rotates through spin phases Ωt , an observer samples a range of instantaneous viewing angles θ_v during its period:

$$\cos \theta_v = \sin \alpha \cos(\Omega t) \sin \zeta + \cos \alpha \cos \zeta \quad , \quad \zeta = \alpha + \theta_{v0} \quad . \quad (65)$$

In this relation, ζ is the observer viewing angle satisfying $\cos \zeta = \hat{\boldsymbol{\Omega}} \cdot \hat{\mathbf{n}}_v$. Thus, θ_{v0} is the viewing angle relative to $\hat{\boldsymbol{\mu}}$ at rotational phases $\Omega t = 2n\pi$, with $n = 0, \pm 1, \pm 2, \dots$. It is now apparent that when this result is inserted into Eq. (64), and the result used to specify $B_E = |\mathbf{B}_E|$, that the phase dependence of the expression for the effective maximum energy due to resonant Compton scattering in Eq. (62) can be mapped throughout the pulse period $0 \leq t \leq 2\pi/\Omega$. Clearly, this maximum upscattering energy is identical for both meridional and antimeridional loops. Yet, the model spectra and pulse profiles of hard X-rays in magnetars may not possess such a symmetry if the activation of the magnetosphere is not uniform in magnetic latitude — such is the case if the densities and/or energies of electrons emanating from footpoints in the two hemispheres differ. For the purposes of the discussion here, it is assumed that the magnetosphere is uniformly activated on a toroidal surface defined by field loops with the same value of r_{\max} , with the

intersection of the toroid and the stellar surface forming two circles of footpoints at colatitudes θ_{\min} and $\pi - \theta_{\min}$.

To illustrate the potential role of photon splitting in attenuating X-rays and γ -rays produced by the resonant Compton upscattering mechanism, Fig. 8 depicts the maximum resonant Compton energy ε_f^{\max} according to Eq. (62), applicable to both polarization states, \perp and \parallel , together with the escape energies $\varepsilon_{\text{esc}}^{sp}$ for the $\perp \rightarrow \parallel$ mode of photon splitting. The splitting escape energies are computed specifically at the resonant Compton interaction colatitudes in Eq. (64) where the Doppler boosting leading to emission up to around ε_f^{\max} is obtained; these $\varepsilon_{\text{esc}}^{sp}$ values were determined using the empirical formula given in Eq. (76) in the Appendix, which applies to curves in Fig. 5. We focus here on photon splitting, since it can attenuate at energies below the absolute pair threshold $2m_e c^2$ that are pertinent to the turnovers in magnetar persistent tail emission: for comparison, the maximum energy of ~ 230 keV detected from 4U 0142+61 is marked on the left axis. The choice of γ_e and B_p is identical to that used for the resonant Compton ε_f^{\max} modulation profiles exhibited in Fig. 5 of Wadiasingh et al. (2018). However, a lower value of $r_{\max} = 5$ is chosen here to connect to Fig. 5 and to accentuate the potential influence of splitting attenuation on phase-resolved emission signatures. Results are exhibited for three different rotator magnetic inclination angles $\alpha = \{15^\circ, 45^\circ, 75^\circ\}$.

Solid curves represent the ε_f^{\max} traces when unattenuated, and the dashed portions of these constitute rotational phases where $\varepsilon_{\text{esc}}^{sp} < \varepsilon_f^{\max}$ and attenuation of \perp polarizations is guaranteed. The dotted curves define $\varepsilon_{\text{esc}}^{sp}$ for splitting. The rotational modulations of both ε_f^{\max} and $\varepsilon_{\text{esc}}^{sp}$ are illustrated for five choices of the observer viewing angle ζ , as labelled using $\theta_{v0} = \zeta - \alpha$. For select values of θ_{v0} , both sets of curves possess gaps, constituting phases where the Doppler-boosted emission on meridional/antimeridional field lines samples zones inside the neutron star, i.e. when $\theta_E > \theta_{\max}$ or $\theta_E < \theta_{\min} \approx 0.1476\pi \approx 26.57^\circ$ (for $r_{\max} = 5$). The dots at the extremities of these gaps (the ends of the curves) thus signify scattering locales that are coincident with field line footpoints on the stellar surface. Note that there will still be emission at the phases corresponding to the gaps in the curves, but that it will be primarily at energies substantially below the values of ε_f^{\max} at the footpoints, since it will correspond to signals not Doppler-boosted along the field lines. Observe also that the particular case of $\alpha = 15^\circ$, the $\theta_{v0} = 150^\circ$ result permits no solutions outside the neutron star, for either hemisphere. This is because the rotator is almost aligned, and the observer's viewing angle is almost polar throughout the period so that scattering locales with the required Doppler beaming along $\hat{\mathbf{n}}_v$ are restricted to very small radii with supercritical fields.

The various loci possess a wealth of information worth highlighting. Two distinctive features of the plots are immediately apparent. The first is that between the meridional and antimeridional cases, for each of the α values there is a large disparity in photon splitting escape energies when averaged over spin phase. This asymmetry between northern and southern hemispheres is expected from the skewness of the curves exhibited in Fig. 5 that address emission tangent to field loops: antimeridional scattering points with $\theta_E > \pi/2$ will generally possess lower escape energies since they sam-

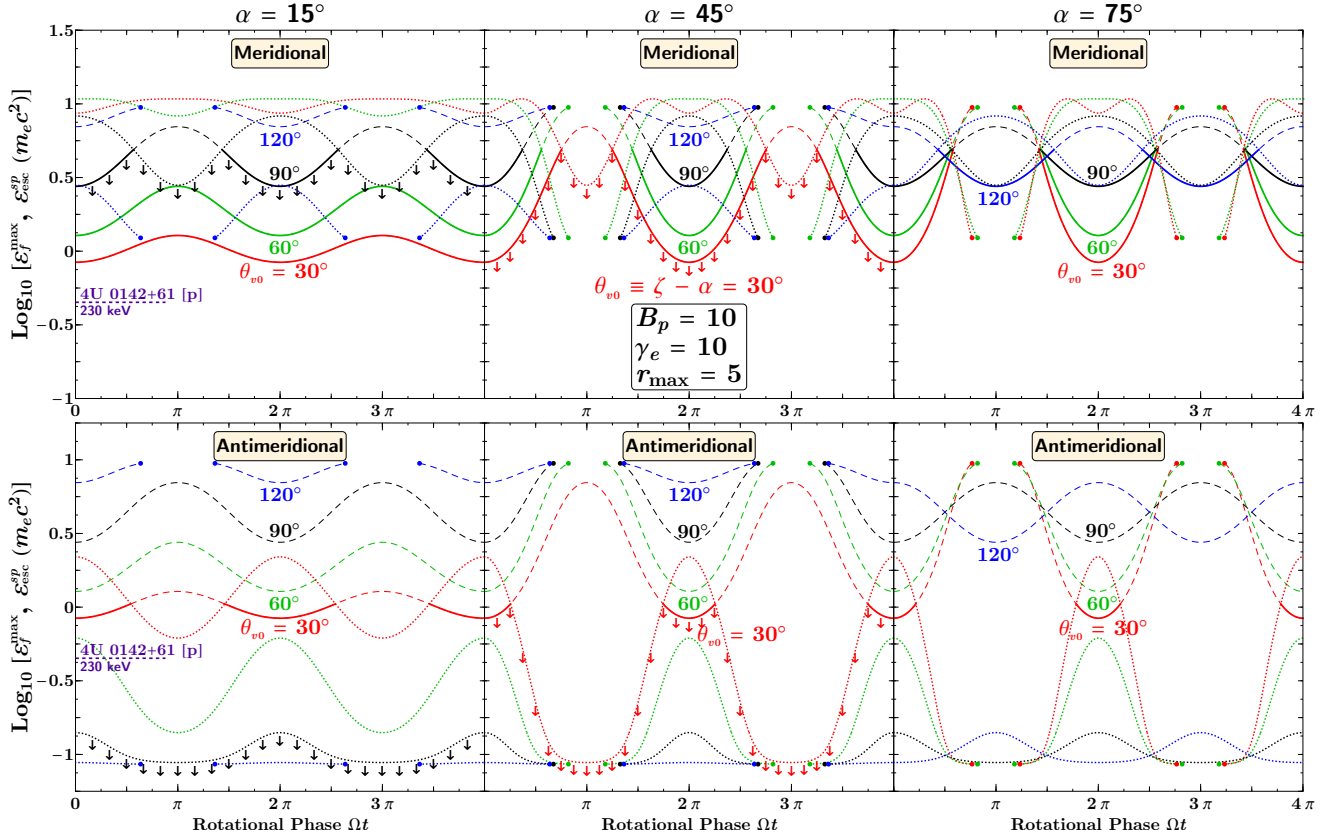


Figure 8. Photon splitting escape energies (dotted curves; $\varepsilon_{\text{esc}}^{\text{sp}}$) for $\perp \rightarrow \parallel$ and resonant Compton maximum cutoff energy $\varepsilon_f^{\text{max}}$ (solid and long-dashed) as functions of spin phase Ωt , for oblique rotators with $\alpha \equiv \arccos(\hat{\Omega} \cdot \hat{\mu}) = \{15^\circ, 45^\circ, 75^\circ\}$. The first and second rows of panels correspond to meridional and antimeridional loops, respectively. In each panel, curves are depicted for several choices of the particular observer viewing angle $\theta_{v0} = \zeta - \alpha$ at phase zero ($\cos \Omega t = 1$), as labeled and color-coded. The $\varepsilon_f^{\text{max}}$ emission energies are depicted as solid curves if $\varepsilon_f^{\text{max}} < \varepsilon_{\text{esc}}^{\text{sp}}$ and long-dashed loci when the inequality is violated and \perp photons are attenuated in a range of energies below $\varepsilon_f^{\text{max}}$. Abrupt termination of curves at the dots marks emission at field line footpoints, demarcating gaps that constitute subsurface locales. Also, the downward arrows mark four sample profiles for effective maximum energies observed in the \perp state, signifying $\min\{\varepsilon_f^{\text{max}}, \varepsilon_{\text{esc}}^{\text{sp}}\}$. See text for details.

ple downward propagation into regions with stronger fields and shorter radii of field curvature. A consequence of this property is that even if the two hemispheres are equally activated with electron distribution profiles that are symmetric in magnetic latitude and uniform in magnetic longitude, an observer will discern a phase dependence in the spectral shape near the maximum energies that signals the action of attenuation due to photon splitting. If Adler's selection rules for splitting apply, then there will also be a strong polarization dependence to this effect — the phase-dependent attenuation will emerge in the \perp state only, and this happens to be the dominant polarization state for resonant upscattering near $\varepsilon_f^{\text{max}}$ (Baring & Harding 2007; Wadiasingh et al. 2018). In contrast, if all polarization modes of splitting can proceed, the splitting $\varepsilon_{\text{esc}}^{\text{sp}}$ curves will move down slightly (see Fig. 5 for a general indication). Then the spectral attenuation at select pulse phases will be more pronounced, yet the polarization dependence of this shaping of a spectral turnover will be weaker. These attenuation nuances for the resonant Compton model are being explored in Wadiasingh et al. (in prep.). Note that since turnovers are not cleanly observed in X-ray tail data for various magnetars, the statistical quality of phase-resolved observations at the maximum energies is presently insufficient to explore these

types of signatures. Accordingly, probes of this information define potential science agendas for planned missions such as AMEGO² and e-ASTROGAM (see De Angelis et al. 2017); see the case argued in detail in Wadiasingh et al. (2019).

The second noticeable characteristic of Fig. 8 is the strong anti-correlation between $\varepsilon_f^{\text{max}}$ and $\varepsilon_{\text{esc}}^{\text{sp}}$: phases where the maximum upscattering resonant energy is greatest coincide with phases where the splitting escape energy is the lowest, i.e. opacity is the highest. This feature is easily understood as a consequence of large $\varepsilon_f^{\text{max}}$ in Eq. (62) corresponding to scattering locales in high fields, i.e. comparatively near the footpoints of field lines, precisely the locations where the escape energies for splitting are the lowest in Fig. 5. This anti-correlation enhances the ability of photon splitting to attenuate hard X-rays generated by resonant Compton upscattering, especially for the antimeridional hemisphere; the same coupling would arise for pair creation escape energies, albeit at energies above $2m_e c^2$. Inspection of the combined splitting/pair creation escape energy depictions in Fig. 10 indicates that pair creation lowers the overall ε_{esc} values at high altitudes along field loops near the equator. In the phase-modulated illustration

² see <https://asd.gsfc.nasa.gov/amego/index.html>.

in Fig. 8, this would manifest itself as a modest lowering of the dotted zones around the peaks of the ε_{esc} curves. Thus, the main impact of adding pair creation opacity is to slightly broaden the phase intervals where opacity curtails the maximum possible energy in $\varepsilon_{\text{esc}} > 2$ domains, and then essentially exclusively in the meridional examples.

A third, related property is that as the rotator obliquity increases from $\alpha = 15^\circ$ to $\alpha = 45^\circ$, the amplitude of the $\varepsilon_f^{\text{max}}$ and $\varepsilon_{\text{esc}}^{\text{sp}}$ modulations increases, though it appears to saturate at even larger obliquities. This is a signature of how a viewer selectively samples the magnetosphere at different rotational phases subject to the Doppler beaming restriction in Eq. (63). As α increases from small values, larger portions of the $r_{\text{max}} = 5$ loops provide access to the condition of tangency for the \hat{n}_v vector, thereby generating more extensive ranges of field strengths sampled. This manifests itself as an increase in the modulations, but once a full sampling of the toroidal loop surface is enabled, at $\alpha \sim 45^\circ$, no further rise in the scale of the modulations is observed when the rotator obliquity continues to increase. While not illustrated here, modulation traces for larger values of r_{max} do exhibit (i) swings with greater ranges of $\varepsilon_f^{\text{max}}$ (see Fig. 5 of Wadiasingh et al. 2018) and $\varepsilon_{\text{esc}}^{\text{sp}}$ due to the increase in field strength ranges spanned by a loop, and (ii) both lower mean values of $\varepsilon_f^{\text{max}}$ and higher means for $\varepsilon_{\text{esc}}^{\text{sp}}$ because the larger loops possess lower fields on average. As a result, the extent of attenuation by splitting is reduced substantially for meridional cases when r_{max} is somewhat larger, but only marginally so for the antimeridional hemisphere.

It is also insightful to focus on the character of the modulation curves for individual choices of the viewer ‘‘impact angle’’ θ_{v0} . Generally, at a particular spin phase, three cases pertaining to opacity configurations are identifiable: (O: opaque) both antimeridional and meridional escape energies are lower than $\varepsilon_f^{\text{max}}$, and thereby the \perp -mode is attenuated near the cut-off $\varepsilon_f^{\text{max}}$, (S: semi-opaque) only the antimeridional emission is split while the meridional one escapes, and (T: transparent) neither meridional/antimeridional escape energies are low enough to be constraining, and the emission from the toroidal surface is transparent to photon splitting. As noted above, if only the \perp polarization splits, cases O and S should evince relatively high polarization degree, nearly $\sim 100\%$, at the spectral cut-off. Unsurprisingly, choices of higher B_p or lower r_{max} than depicted in Fig. 8 generally result in cases O and S presenting throughout most rotational phases. As an intermediate example, case O transpires for the $\theta_{v0} = 90^\circ$ choice for a range of phases near $\cos\Omega t = -1$ for all the α columns of Fig. 8, but not for other rotational phases. At these phases, the instantaneous θ_v is generally large and the emission colatitude in Eq. (64) is proximate to the magnetic footpoints. Likewise, the $\theta_{v0} = 30^\circ$ example exhibits phases of case S and case T, accompanied by phase-resolved polarization degrees that vary strongly as the signal transitions from transparency to opacity for the photon splitting mode $\perp \rightarrow \parallel$. Interestingly, a pulse profile may present all three configurations O, S and T depending on rotational phase, an obvious example being provided by $\theta_{v0} = 30^\circ$ for the $\alpha = 45^\circ$ case.

As a cautionary note accompanying the results presented in this subsection, the highlighted signatures should not be over-interpreted. In reality, resonant Compton up-scattering emission involves a convolution of various r_{max}

toroidal surfaces (e.g., see Wadiasingh et al. 2018) and Lorentz factors for electrons populating the magnetosphere, both of which will blur the features identified here. Moreover, for some rotational phases the resonant spectrum is effectively suppressed because the local resonance condition samples soft photon energies ε_s above the Planck mean of $3kT$, and this can move the luminous part of the up-scattering signal to well below the escape energy $\varepsilon_{\text{esc}}^{\text{sp}}$. In addition, excursions from dipolar field morphology such as those predicted in twisted field models (e.g. Chen & Beloborodov 2017) will complicate the phase dependence of $\varepsilon_f^{\text{max}}$ and $\varepsilon_{\text{esc}}^{\text{sp}}$ substantially, introducing higher-order asymmetries. Notwithstanding, if the highlighted phase-resolved polarimetric characteristics are detected by future hard X-ray spectrometers and polarimeters, they would help confirm the action of photon splitting in Nature. In particular, signatures such as ones highlighted here offer a path to constraining both the magnetar geometry parameters $\{\alpha, \zeta\}$, and the particle Lorentz factor γ_e distribution, and also which r_{max} bundles contribute to the total emission.

5 GENERAL RELATIVISTIC INFLUENCES

To complete this exposition on photon splitting and pair creation opacity in magnetar magnetospheres, it remains to explore how curved spacetime at low altitudes impacts the escape energies. Since such general relativistic (GR) effects have already been identified at length in the papers of Harding, Baring & Gonthier (1997); Baring & Harding (2001); Story & Baring (2014), the presentation here will be limited. While light bending and its change in frequency imposed by the curvature of spacetime are familiar concepts, the non-Euclidean metric distorts the mathematical form of a dipole magnetic field (Petterson 1974; Wasserman & Shapiro 1983; Gonthier & Harding 1994), altering the field line shape and increasing the strength of the field. All these modifications combine to alter the rates for any QED process involving photons in strongly-magnetized neutron star environs. The interplay between the GR magnetic geometry and the GR photon ray-tracing is important to identify, since this captures complete information on the vector values of the field \mathbf{B}_{GR} and the photon momentum \mathbf{k}_{GR} at each locale that are needed for precise determination of the opacity.

5.1 General Relativistic Opacity Construction

The general relativistic construction in this paper follows that laid out in detail in Story & Baring (2014). The optical depth is obtained as an integration over the geodesic path length variable s , with the attenuation coefficient specified at each point in the local inertial frame (LIF) in terms of the variables B , ω and Θ_{KB} . The expressions for these are posited without derivation. The simplest quantity to specify is obviously the LIF photon energy ω ,

$$\omega = \frac{\varepsilon}{\sqrt{1 - \Psi}} \quad , \quad \Psi = \frac{r_s}{r} \equiv \frac{2GM}{c^2 r} \quad (66)$$

at radius r , where $r_s = 2GM/c^2$ is the Schwarzschild radius of a neutron star of mass M . This expresses the blueshift of the photon energy ε observed at infinity. Throughout this section, we will set $M = 1.44M_\odot$. The proxy radius parameter Ψ facilitates the specification of all

pertinent general relativistic quantities, and will be used as the variable for the path integration.

The general relativistic form of a dipole magnetic field in a Schwarzschild metric was expounded in Wasserman & Shapiro (1983); Muslimov & Tsygan (1986); Gonthier & Harding (1994). Its evaluation in the LIF can be expressed in a compact form

$$\mathbf{B}_{\text{GR}} = 3 \frac{B_p \Psi^3}{r_s^3} \left\{ \xi_r(\Psi) \cos \theta \hat{r} + \xi_\theta(\Psi) \sin \theta \hat{\theta} \right\} \quad (67)$$

by defining field component functions

$$\begin{aligned} \xi_r(x) &= -\frac{1}{x^3} \left[\log_e(1-x) + x + \frac{x^2}{2} \right] \\ \xi_\theta(x) &= \frac{1}{x^3 \sqrt{1-x}} \left[(1-x) \log_e(1-x) + x - \frac{x^2}{2} \right]. \end{aligned} \quad (68)$$

For Euclidean geometry, corresponding to $\Psi \ll 1$, the leading terms of Taylor series expansions yield $\xi_r(\Psi) \approx 1/3$ and $\xi_\theta(\Psi) \approx 1/6$, so that then Eq. (67) reproduces the familiar result in Eq. (3). When Ψ is not small, in general the ξ_r, ξ_θ exceed these values and the magnitude of the magnetic field in the LIF is increased by the curvature of spacetime.

The curved photon geodesic can be identified once the initial momentum at the emission point is specified. To illustrate the key influences of general relativity on splitting and pair creation opacity determinations, we restrict considerations to light propagation in a plane constituted by a single magnetic longitude, a protocol adopted by Story & Baring (2014). The momentum therefore possesses no ϕ component and can be specified at any point by \hat{r} and $\hat{\theta}$ coordinate vectors, just like the magnetic field in this plane. This provides a convenient simplification of the GR (\mathbf{k}, \mathbf{B}) geometry algebra. For this configuration, and indeed for all photon orbits in a Schwarzschild geometry, a photon's path at infinity moves parallel to a straight line drawn from the center of the star, with the path displaced from it by a distance b . This impact parameter b is proportional to the ratio of the orbital angular momentum and the energy, both being conserved along the photon trajectory. Typical geometry is illustrated in Pechenick, Ftaclas & Cohen (1983), or in textbooks such as Shapiro & Teukolsky (1983).

Scaling b by the Schwarzschild radius, as we have with r , introduces a new trajectory parameter $\Psi_b = r_s/b$ that can be related to emission point parameters Ψ_E and θ_E for the specific case of the dipole field via

$$\Psi_b = \Psi_E \sqrt{(1 - \Psi_E) \left\{ 1 + [\xi(\Psi_E)]^2 \cot^2 \theta_E \right\}} \quad , \quad (69)$$

where

$$\xi(\Psi) = \frac{\xi_r(\Psi)}{\xi_\theta(\Psi)} \quad . \quad (70)$$

This functional relationship $\Psi_b(\Psi_E, \theta_E)$ applies only for the special case of photon emission parallel to the local magnetic field, the major focus of Section 4.2 that is motivated therein. The textbook photon orbit equation is an integral equation that expresses the change in polar angle in terms of the path's radial parameter Ψ , namely

$$\theta(\Psi) \equiv \theta_E + \Delta\theta = \theta_E \pm \int_{\Psi}^{\Psi_E} \frac{d\Psi_r}{\sqrt{\Psi_b^2 - \Psi_r^2(1 - \Psi_r)}} \quad . \quad (71)$$

This expresses the dependence $\theta(r)$ as viewed by an observer at infinity. There are two branches to this solution of

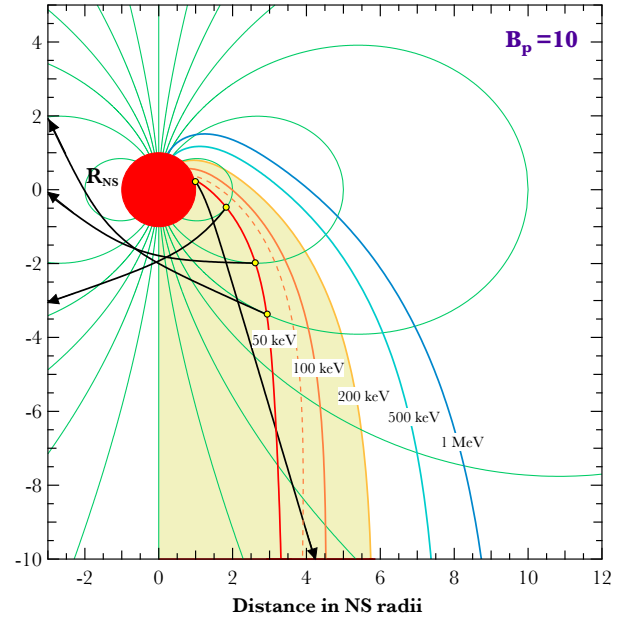


Figure 9. A “splittosphere” diagram of opacity for a magnetar with $M = 1.44M_\odot$, $R = 10^6$ cm and $B_p = 10$, for photon propagation in the Schwarzschild metric that is coplanar with a nested set of dipolar field lines (depicted in light green). The (x, z) coordinates (as in Fig. 1) are scaled by neutron star radii and the central red solid unit circle represents the neutron star. Colored contours represent the lowest possible emission altitude for transparency at a given colatitude, for a photon of a fixed energy (as labeled) that is emitted parallel to the local \mathbf{B} and away from the upper pole. Inside these contours, the magnetosphere is opaque to the $\perp \rightarrow \parallel$ mode of photon splitting; the yellow shaded region indicates the zone of opacity for photons with an energy of 200 keV. The dashed orange contour is a flat spacetime version of the 100 keV case. Photon trajectories are plotted for selected emission points on the 50 keV contour as black curves with arrows. The curvature of these geodesics in general relativity is determined using Eq. (71) and its adaptation beyond periastron passage.

the geodesic equation, and these are bifurcated by the periastron point $\Psi = \Psi_p$ where the radius is a minimum. This location corresponds to $d\theta/dr = -(\Psi/r)d\theta/d\Psi \rightarrow \infty$, so that $\Psi_b^2 = \Psi_p^2(1 - \Psi_p)$. For an outward-propagating photon, the branch with the positive sign in Eq. (71) is applicable. For inward propagation, the negative sign is chosen at first. In that case, if the photon passes through periastron, the subsequent portion of outward propagation employs the positive sign, starting from Ψ_p instead of Ψ_E , and adds two $\Delta\theta$ contributions in a piecewise fashion. Examples of three periastron transit trajectories where this construction is applied are illustrated in Fig. 9.

The exact calculation of the photon trajectory requires a time-consuming numerical integration, motivating the use of suitable analytic approximations. While the series evaluation technique of Story & Baring (2014) works well for quasi-polar emission locales, something more widely applicable is needed to treat periastron passage. The “cosine relation” provided by Beloborodov (2002) gives an accurate approximation, relating the photon's radius, its direction and the polar angle, from which we can obtain an analytic form of $\theta(\Psi)$. Beloborodov's formula works with $\sim 1\%$ accuracy for $\Psi < 0.5$, which suffices for our calculations here.

From the foregoing elements, one can assemble the last important ingredient for opacity calculations, namely the angle Θ_{kB} between the photon momentum \mathbf{k}_{GR} and the magnetic field \mathbf{B}_{GR} in the LIF. The photon momentum is posited in Eq. (A1) of Harding, Baring & Gonthier (1997), and is directly derivable from the path equation via $k_\theta/k_r = d\theta/dr$, the approach of Story & Baring (2014). Thus, for photons moving away from the star ($0 < \theta_E < \pi/2$),

$$\mathbf{k}_{\text{GR}} = \frac{\varepsilon}{\Psi_b \sqrt{1 - \Psi}} \left\{ \sqrt{\Psi_b^2 - \Psi^2(1 - \Psi)} \hat{r} + \Psi \sqrt{1 - \Psi} \hat{\theta} \right\} \quad (72)$$

in the local inertial frame, with a magnitude that captures the blueshift of the photon energy relative to that perceived at infinity. Forming the cross product of this with Eq. (67), one soon arrives at

$$\sin \Theta_{\text{kB}} = \frac{\sqrt{\Psi_b^2 - \Psi^2(1 - \Psi)} - \Psi \sqrt{1 - \Psi} \xi(\Psi) \cot \theta}{\Psi_b \sqrt{1 + [\xi(\Psi)]^2 \cot^2 \theta}} \quad (73)$$

an expression that is also obtained by rearranging Eq. (37) of Gonthier & Harding (1994). Employing the form for Ψ_b in Eq. (69) quickly reveals that when $\Psi = \Psi_E$, this expression yields $\sin \Theta_{\text{kB}} = 0$. For light emitted in the lower hemisphere, $\pi/2 < \theta_E < \pi$, a change of sign appears in the \hat{r} term in Eq. (72), and thus also in the first term of the numerator of Eq. (73). Since then $\cot \theta$ is negative, one again observes that $\sin \Theta_{\text{kB}} = 0$ at the point of emission.

The opacity integral can be formed using the pathlength element $ds = \sqrt{1 - \Psi} c dt$ in the LIF, in which the coordinate time element dt can be expressed in terms of observer frame coordinates using formulae for Shapiro delay. A change of variables to Ψ is expedient, and the details are given in Story & Baring (2014). The optical depth in this general relativistic formulation takes the form

$$\tau(\Psi) = r_s \int_{\Psi}^{\Psi_E} \frac{\mathcal{R}(\omega, \sin \Theta_{\text{kB}}, |\mathbf{B}_{\text{GR}}|) \Psi_b d\Psi_r}{\Psi_r^2 \sqrt{(1 - \Psi_r) \{\Psi_b^2 - \Psi_r^2(1 - \Psi_r)\}}} \quad (74)$$

where the arguments of the quantum pair creation attenuation coefficient \mathcal{R} are given by Eqs. (66), (67) and (73). One then formally defines the attenuation length L as in Harding, Baring & Gonthier (1997) and Baring & Harding (2001) via

$$\tau(\Psi_L) = 1 \quad ; \quad s(\Psi_L) = L \quad . \quad (75)$$

L is approximately the cumulative LIF distance that a photon will travel from its emission point before being attenuated. As before, the escape energy ε_{esc} is defined by the condition $L \rightarrow \infty$, i.e. $\Psi_L \rightarrow 0$.

Using this formalism, a variety of opacity results were generated, most of which were designed as checks on the construction and numerics and are not presented here, since our focus is on highlighting the main influences of general relativity. First among these checks were comparisons with the results of Story & Baring (2014): the new C codes developed here for computing the opacity in Eq. (74) reproduced the pair creation attenuation lengths presented in Fig. 5 and the escape energies in Figs. 6 and 7 of that paper with excellent precision. To appraise the photon splitting GR opacity numerics, we compared escape energies with those illustrated for surface emission in Fig. 1 of Baring & Harding

(2001), which were systematically around 20% lower than our determinations at colatitudes greater than around 5–10 degrees when photons were emitted initially parallel to \mathbf{B} ($\Theta_e = 0$). Approximately the same offset applied to pair creation opacity also, and our numerical results again agreed with those generated by Story & Baring (2014). In contrast, for $\Theta_e = 0.01$, when $\theta_E \lesssim 1^\circ$, there was good agreement between our computations and the values of ε_{esc} in Fig. 1 of Baring & Harding (2001) for both attenuation processes.

The numerical evaluation of $\sin \Theta_{\text{kB}}$ was suggested by Story & Baring (2014) as the possible origin of the discrepancy at $\theta_E \gtrsim 1^\circ$, since their determinations of $\sin \Theta_{\text{kB}}$ agreed with those in Fig. 5 of Gonthier & Harding (1994), yet are smaller by around 20% relative to those in Harding, Baring & Gonthier (1997). Our codes here nicely reproduce the $\sin \Theta_{\text{kB}}$ results of both Gonthier & Harding (1994) and Story & Baring (2014). A very recent inspection of the old propagation codes used in Harding, Baring & Gonthier (1997); Baring & Harding (2001) has revealed a factor of 2 bug in the photon ray-tracing (in Eq. (A2) of Harding et al. (1997), the first m should be $2m$). This has been corrected, thereby bringing the numerical evaluations from this old independent code into excellent agreement with the escape energies presented here and in Story & Baring (2014).

5.2 Opacity Volumes and Escape Energies

The general relativistic construction was used to develop an illustration of the geometry of regions of opacity for photon splitting in the magnetosphere of a $B_p = 10$ magnetar, which is presented in Fig. 9. This represents a planar (meridional) section of azimuthally-symmetric volumes of opacity/transparency, for the case of photons emitted parallel to field lines at positions $x > 0$ and directed away from the upper (northern) pole. For a selection of photon escape energies $\varepsilon_{\text{esc}} = 50, 100, 200, 500, 1000$ keV as observed at infinity, the depicted contours separate the zones of opacity in the interior from the outer regions of transparency where the field is lower on average. The opacity volumes, termed the “**splittosphere**,” extend down to the magnetic axis of symmetry at large colatitudes, or the stellar surface at small colatitudes. A cross section of the splittosphere for the 200 keV case is identified by the shaded yellow region inside the corresponding surface contour. Photons emitted inside these regions with energies larger than the labeled energies are subject to splittings $\perp \rightarrow \parallel$. Similar volumes would arise for the other modes of splitting if they are permitted. These volumes, which somewhat resemble cometary tails, decrease in flat spacetime (see the dashed curve for 100 keV) and obviously decrease with the increase of photon energy in accord with the rates in Eq. (23).

The splittosphere contours are asymmetric about the x axis, because it is assumed that the leptons flow from north (upper) pole to south (lower) pole. If leptons transit field loops in both directions, a mirror image opacity zone would also arise with a reflection of the one in Fig. 9 about the x axis. It is noticeable that each contour here realizes an asymptote that is approximately parallel to the z axis and extends downwards to infinity at colatitudes $\pi > \theta_E > \pi/2$ where inward emission prevails. While the field strength at the emission point drops well below the critical value in

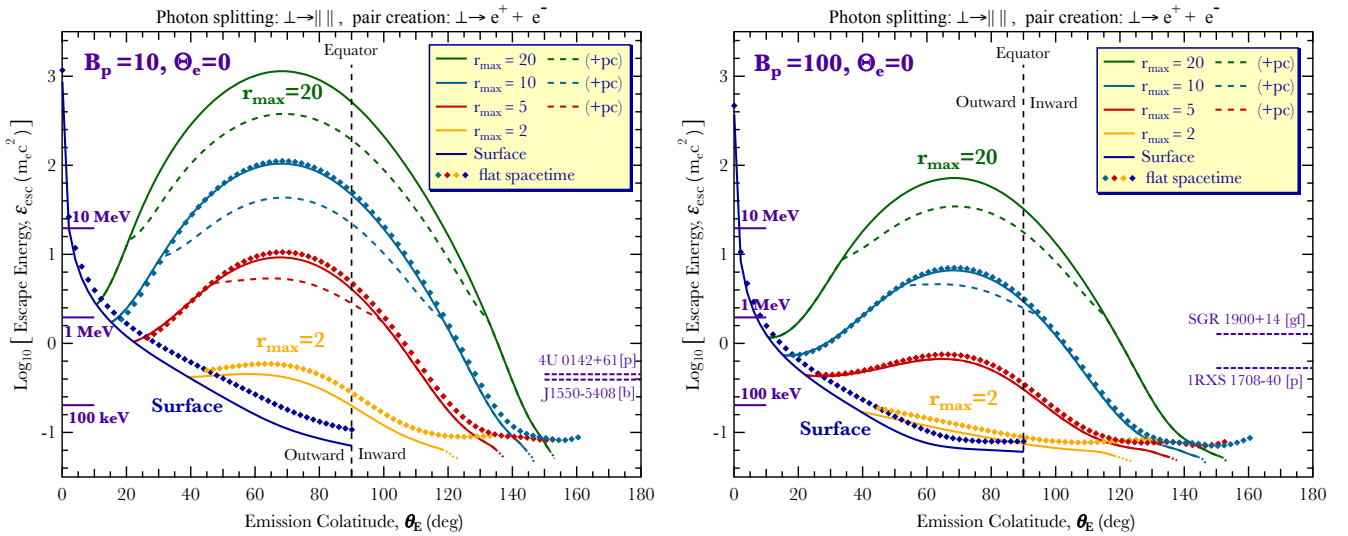


Figure 10. Escape energies for photon splitting (mode $\perp \rightarrow \parallel$, solid curves) and also when adding pair creation of the \perp state to the total opacity (+pc, dashed curves), for maximum loop altitudes $r_{\max} = 2, 5, 10, 20$ in units of R_{NS} . All determinations are for general relativistic propagation, except for those denoted as being for flat spacetime, namely the traces of diamonds for the surface and $r_{\max} = 2, 5, 10$ examples. A meridional specialization with photon emission initially parallel to the local magnetic field line ($\Theta_e = 0$) is adopted, as in Figs. 5 and 6, with the left and right panels for surface polar fields $B_p = 10$ and $B_p = 100$, respectively. The surface emission curves for both curved and flat spacetimes are truncated at the equator (outward emission only). Other aspects of the display such as shadowing portions and the magnetar marker energies are as in Figs. 5 and 6. As θ_E increases in transiting from footpoint to the opposite footpoint, the escape energy traces first a splitting evaluation (solid), then to a lower pair creation determination (dashed, at equatorial colatitudes), and back to a splitting evaluation (inward propagation as depicted in Fig. 9); see text for details.

these locales, the photon trajectory passes close to the stellar surface where the field is intense and Θ_{KB} is also large. In such cases, the dominant contribution to the opacity arises near and at periastron passage and can be substantial. This is the reason why the escape energy contours do not merge with the z -axis at finite values of the x coordinate.

While Fig. 9 applies to photon emission along field lines as typically arises for Doppler-boosted mechanisms, one can quickly discern the general character of modifications to the splittosphere morphology for non-zero emission angles Θ_e . Inspection of the left panel of Fig. 7 reveals that at low colatitudes somewhat near the north pole, the escape energies generally drop as Θ_e increases above zero, while in the lower magnetic hemisphere ε_{esc} is reduced in the $\zeta_E = 0$ cases exhibited, signalling higher opacity; a reduction in opacity arises in $\zeta_E = 180^\circ$ cases. Accordingly, one anticipates that in the upper hemisphere of Fig. 9 at colatitudes $\theta_E < \pi/2$, the zones of opacity will bulge somewhat. In the lower, $\pi/2 < \theta_E < \pi$ hemisphere, the splittosphere will shrink or expand depending on the direction of emission relative to the local \mathbf{B} . Generally, in such cases, photon trajectories with larger periastron radii will sample lower fields and lower opacities on average, and therefore yield smaller regions for opaque conditions.

The impact of general relativity on the determination of escape energies can be identified via plots like those in Figs. 5 and 6. To streamline this information, we now combine photon splitting and pair creation escape energies graphically in Fig. 10, where the y -axis represents the escape energy as perceived by an observer at infinity. Solid curves represent escape energies for photon splitting. Dashed curves correspond to a combination of pair creation and photon splitting, being clearly visible for colatitudes θ_E where the pair creation escape energy is lower than that for splitting; hence

the (+pc) designation in the legends. Only results for the \perp polarization are exhibited in Fig. 10, and similar character would appear for the \parallel state, provided that all three CP-permitted modes of splitting operate. The surface emission curves are depicted only for outward photon emission into the magnetosphere, i.e. truncated at the equator.

Flat spacetime curves are depicted for the surface emission and $r_{\max} = 2, 5, 10$ examples as well as the GR ones to demonstrate how for most emission locales, general relativity reduces ε_{esc} , by a factor of up to two at $r_{\max} < 2$, and by around 10–20% for $r_{\max} = 10$. This ε_{esc} reduction is a direct consequence of the increase in field strength and the photon energy in the local inertial frame in the Schwarzschild metric. Accordingly, GR upgrades modify the constraints on the possible emission volumes only modestly, as depicted in Fig. 9. Another feature of the plots is that the range of colatitudes for which pair creation is dominant is more restricted for the $B_p = 100$ case. This behavior follows from photon splitting being more effective at lower energies than pair creation. Comparison of the footpoint colatitudes for the loop $r_{\max} = 2$ examples in flat and curved spacetime in the northern hemisphere ($\theta_E < \pi/2$) illustrates how, when r_{\max} is held fixed, general relativity moves the footpoints closer to the pole as the field there intensifies. A more subtle signature of the Schwarzschild metric that appears in Fig. 10 is the fact that the endpoint colatitudes of the loop curves are not symmetrically spaced about the equator: the inward portions end at colatitudes more remote from the southern pole than the actual field line footpoint near the northern pole. This is a consequence of the strong curvature of photon trajectories, as depicted in Fig. 9. As the impact parameter b declines, capture orbits can be realized, for which unattenuated photons cannot escape; this phenomenon prescribes the truncation colatitude of the curves.

6 CONCLUSIONS

In this paper, opacities for photon splitting and pair creation have been calculated in the magnetospheres of neutron stars, with an emphasis on magnetars. Attenuation lengths and escape energies, the maximum energies for transparency from the emission point to infinity, are computed for emission locales that are not exclusively tied to the stellar surface or the magnetic poles. The presentation attaches special significance to loop emission cases, which are more closely connected to physical emission models: in slowly-rotating magnetars, motion of relativistic charges along field lines introduces strong Doppler beaming of the radiation. Our calculations indicate that photon splitting dominates high energy photon attenuation for supercritical field strengths, while in the slightly subcritical field domain, pair creation is more often the leading attenuation mechanism.

For both persistent signals and flares in magnetars, photon splitting attenuation alone puts constraints on the possible emission locales in their magnetospheres when accommodating the maximum observed energies. For $B_p = 10$ cases, magnetospheric regions within loops of maximum altitudes $r_{\max} \lesssim 2$ (scaled in neutron star radii) are completely forbidden by splitting attenuation opacity for persistent emission with energy above around 230 keV. For the $r_{\max} = 5$ loop case, emission regions with $\theta_E > 115^\circ$ are excluded by splitting. The inherent asymmetry comes from the restriction of leptons moving along field lines from the northern (i.e., low θ_E) to the southern ($\theta_E \sim 180^\circ$) magnetic footpoints when generating high-energy photons. The inward emission at high colatitudes propagates into southern polar regions with strong fields and shorter radii of field curvature, so that the opacities increase accordingly. Similarly, for $B_p = 100$ cases, magnetospheric regions with $r_{\max} \lesssim 4$ are completely forbidden for persistent emission with energy above around 270 keV, and the $r_{\max} = 5$ loop is permitted at low colatitudes with $\theta_E < 85^\circ$. In Section 5, general relativistic modifications are addressed, and for most emission locales, it reduces ε_{esc} , by a factor of up to two at low altitudes $r_{\max} \lesssim 2$, and by around 10–20% for $r_{\max} = 10$.

In Section 4.3, a model of attenuation by photon splitting combined with resonant inverse Compton scattering was presented for the case where only photons with \perp polarization can split. This illustrated that the maximum up-scattering (ε_f^{\max}) and escape ($\varepsilon_{\text{esc}}^{sp}$) energies both depend strongly on the pulse phase of the rotating star even when toroidal field bundles are uniformly activated. The asymmetry of the two hemispheres and the anti-correlation between ε_f^{\max} and $\varepsilon_{\text{esc}}^{sp}$ derive strong spectral and polarization signatures, highlighted in Fig. 8. Allowing all CP-permitted polarization modes of splitting to proceed will modify both the spectral and polarization signatures, yet still retaining a richness of potential observational diagnostics; such will be the subject of future study. These signatures, if assessed using future phase-resolved observations from proposed MeV band telescopes such as AMEGO and e-ASTROGAM (e.g., see Wadiasingh et al. 2019), could identify which modes of photon splitting are operating, probe the emission region locale, and help determine the major geometric parameters of the star, i.e. the inclination angle, α , between the magnetic and rotation axes, as well as an observer’s viewing angle, ζ .

ACKNOWLEDGMENTS

The authors thank George Younes and the anonymous referee for suggestions helpful to the polishing of the manuscript. M. G. B. acknowledges the generous support of the National Science Foundation through grant AST-1517550, and NASA’s *Fermi* Guest Investigator Program through grant NNX16AR66G. Z. W. is supported by the NASA postdoctoral fellowship program.

APPENDIX

Empirical Escape Energies for Loop Emission:

The escape energy calculations for loop emission can be directly incorporated in various the emission models for magnetars. The example addressed in Section 4 is the resonant Compton upscattering scenario for hard X-ray tails in magnetars. It is expedient to employ compact analytic approximations for opacity in such models, and so here we assemble empirical fits to escape energies computed in Section 4.2. Well below pair threshold, the photon splitting attenuation coefficient is proportional to ε^5 , thus the optical depth for photons with a energy of ε can be expressed as $\tau = \exp[-(\varepsilon/\varepsilon_{\text{esc}})^5]$. We developed an empirical approximation for the $\perp \rightarrow \parallel$ escape energy for photon emission along field loops, yielding the form

$$\varepsilon_{\text{esc}}^{sp} \approx 5.33 B_p^{-1.2} r_{\max}^{3.4} \frac{\sin^{12.9} \theta_E}{\theta_E^{6.18}} + 0.58 B_p^{-0.5} r_{\max} \exp(-\theta_E^2) + 0.1 B_p^{-0.07} \quad (76)$$

This was designed to best describe the shape of the loop curves exhibited in Figure 5. The first term in Eq. (76) represents the bell-shaped humps, while the second and the third terms deliver corrections for small and large colatitudes, respectively. Eq. (76) works well for large r_{\max} cases, but deviates slightly from numerical results for small r_{\max} emission, i.e. $r_{\max} < 3$. In addition, this formula is also approximately applicable to other splitting modes and the polarization-averaged mode, since their escape energies are similar (see Fig. 5). To apply this to the polarization-averaged case, intuition suggests multiplying the result in Eq. (76) by the factor $[2\mathcal{M}_1^2/(3\mathcal{M}_1^2 + \mathcal{M}_2^2)]^{1/5}$. Since the major portion of the loops is at altitudes where sub-critical fields exist, the \mathcal{M}_σ in this factor can be replaced by constants, yielding a multiplicative factor $(338/1083)^{1/5} \approx 0.792$ for the polarization-averaged escape energy formula.

Similarly, we derived an empirical formula for $\parallel \rightarrow e^+e^-$ mode pair creation based on the results presented in Fig. 6 as well, which is expressed as

$$\varepsilon_{\text{esc}}^{pp} \approx \max \left\{ 2, 2.3 B_p^{-1.05} r_{\max}^{3.1} \frac{\sin^{11.5} \theta_E}{\theta_E^{5.41}} + 1.26 \theta_E^{-1.78/r_{\max}^{0.3}} r_{\max}^{0.5} e^{-\theta_E^2/2} \right\} \quad (77)$$

The piecewise form of the function originates from the horizontal absolute threshold tails in Fig. 6, i.e., $\varepsilon_{\text{esc}}^{pp}$ cannot be lower than the absolute threshold $2m_e c^2$. The empirical formula is not very accurate for low altitude cases where the escape energy curves decrease slightly with increasing emission colatitude. Note this empirical formula is not applicable to the \perp mode creation because of the subsequent dependence of the pair threshold on the field strength.

REFERENCES

- Abdo, A. A. et al. 2010, *ApJS* 187, 460.
- Adler, S. L. 1971, *Ann. Phys.* 67, 599
- Baier, V. N. & Katkov, V. M. 2007, *Phys. Rev. D*, 75, 073009
- Baring, M. G. 1988, *MNRAS*, 235, 51
- Baring, M. G. 1995, *ApJ*, 440, L69
- Baring, M. G. 2000, *Phys. Rev. D*, 62, 016003
- Baring, M. G. & Harding, A. K. 1997, *ApJ*, 482, 372
- Baring, M. G. & Harding, A. K. 1998, *ApJ Lett.*, 507, L55
- Baring, M. G. & Harding, A. K. 2001, *ApJ*, 547, 929
- Baring, M. G. & Harding, A. K. 2007, *Astrophys. Spac. Sci.*, 308, 109
- Baring, M. G., Wadiasingh, Z., & Gonthier, P. L. 2011, *ApJ*, 733, 61
- ter Beek, F. 2012, Masters thesis, University of Amsterdam.
- Beloborodov, A. M. 2002, *ApJ*, 566, L85
- Beloborodov, A. M. 2013, *ApJ*, 762, 13
- Chen, A. Y., & Beloborodov, A. M. 2017, *ApJ*, 844, 133
- Daugherty, J. K. & Harding, A. K. 1982, *ApJ*, 252, 337
- Daugherty, J. K. & Harding, A. K. 1983, *ApJ*, 273, 761
- Daugherty, J. K. & Harding, A. K. 1986, *ApJ*, 309, 362
- Daugherty, J. K. & Harding, A. K. 1996, *ApJ*, 458, 278
- De Angelis, A., Tatischeff, V., Tavani, M., et al. 2017, *Experimental Astronomy*, 44, 25
- Duncan, R. C. & Thompson, C. 1992, *ApJ*, 392, L9
- Erber, T. 1966, *Rev. Mod. Phys.*, 38, 626.
- Fernández, R. & Thompson, C. 2007, *ApJ*, 660, 615
- Feroci, M., Caliendo, G. A., Massaro, E., Mereghetti, S., & Woods, P. M. 2004, *ApJ*, 612, 408
- Feroci, M., Frontera, F., Costa, E., et al. 1999, *ApJ Lett.*, 515, L9
- Gnedin, Yu. N., Pavlov, G. G. & Shibanov, Yu. A. 1978, *Soviet Phys. JETP Lett.*, 27, 305
- Gögüs, E., Woods, P. M., Kouveliotou, C., et al. 1999, *ApJ Lett.*, 526, L93
- Gögüs, E., Woods, P. M., Kouveliotou, C., et al. 2000, *ApJ Lett.*, 532, L121
- Gonthier, P. L., Baring, M. G., Eiles, M. T., et al. 2014, *Phys. Rev. D*, 90, 043014
- Gonthier, P. L. & Harding, A. K. 1994, *ApJ*, 425, 767
- Gonthier, P. L., Harding, A. K., Baring, M. G., et al. 2000, *ApJ*, 540, 907
- Götz, D., Mereghetti, S., Tiengo, A. & Esposito, P. 2006, *A&A*, 449, L31
- Harding, A. K. & Baring, M. G. 1996, *American Institute of Physics Conference Series*, 384, 941
- Harding, A. K., Baring, M. G., & Gonthier, P. L. 1996, *AAPS*, 120, 111
- Harding, A. K., Baring, M. G. & Gonthier, P. L. 1997, *ApJ*, 476, 246
- Harding, A. K., Contopoulos, I. & Kazanas, D. 1999, *ApJ Lett.*, 525, L125
- Harding, A. K. & Lai, D. 2006, *Rep. Prog. Phys.*, 69, 2631
- Harding, A. K. & Kalapotharakos, C. 2015, *ApJ*, 811, 63
- den Hartog, P. R., Kuiper, L., Hermsen, W., et al. 2008a, *A&A*, 489, 245
- den Hartog, P. R., Kuiper, L. & Hermsen, W. 2008b, *A&A*, 489, 263
- Hurley, K., Boggs, S. E., Smith, D. M., et al. 2005, *Nat.*, 434, 1098
- Hurley, K., Kouveliotou, C., Woods, P., et al. 1999, *ApJ Lett.*, 510, L107
- Israel, G. L., Romano, P., Mangano, V., et al. 2008, *ApJ*, 685, 1114
- Klepikov, N. V. 1954, *Zh. Eksp. Theor. Fiz.*, 26, 19
- Kuiper, L., Hermsen, W., den Hartog, P. R. & Collmar, W. 2006, *ApJ*, 645, 556
- Lai, D., & Ho, W. C. G. 2003, *Phys. Rev. Lett.*, 91, 071101
- Li, J., Rea, N., Torres, D. F. & de Oña-Wilhelmi, E. 2017, *ApJ*, 835, 30
- Lin, L., Gögüs, E., Baring, M. G., et al. 2012, *ApJ*, 756, 54
- Lyutikov, M., & Gavriil, F. P. 2006, *MNRAS*, 368, 690
- Mazets, E. P., Golenetskii, S. V., Il'Inskii, V. N., et al. 1979, *Soviet Astronomy Lett.*, 5, 163
- Mereghetti, S. 2008, *A&ARv*, 15, 225
- Mészáros, P. 1992, *High-energy Radiation from Magnetized Neutron Stars*, (University of Chicago Press, Chicago)
- Mészáros, P. & Ventura, J. 1978, *Phys. Rev. Lett.*, 41, 1544
- Muslimov, A. G., & Tsygan, A. I. 1986, *Soviet Astronomy*, 30, 567
- Nobili, L., Turolla, R., & Zane, S. 2008, *MNRAS*, 386, 1527
- Olausen, S. A. & Kaspi, V. M. 2014, *ApJ Supp.*, 212, 6
- Özel, F. 2001, *ApJ*, 563, 276
- Pechenick, K. R., Ftaclas, C. & Cohen, J. M. 1983, *ApJ*, 274, 846
- Pettersson, J. A. 1974, *Phys. Rev. D*, 10, 3166
- van Putten, T., Watts, A. L., Baring, M. G., & Wijers, R. A. M. J. 2016, *MNRAS*, 461, 877
- Romani, R. W. 1996, *ApJ*, 470, 469
- Ruderman, M. A. & Sutherland, P. G. 1975, *ApJ*, 196, 51
- Schwinger, J. 1951, *Phys. Rev.*, 82, 664
- Shabad, A. E. 1975, *Ann. Phys.* 90, 166
- Shapiro, S. L. & Teukolsky, S. A. 1983, *Black Holes, White Dwarfs, and Neutron Stars: The Physics of Compact Objects* (John Wiley & Sons: New York)
- Sokolov, A. A. & Ternov, I. M. 1968 *Synchrotron Radiation*, (Pergamon Press, Oxford)
- Story, S. A. & Baring, M. G. 2014, *ApJ*, 790, 61
- Sturrock, P. A. 1971, *ApJ*, 164, 529
- Thompson, C. & Duncan, R. C. 1995, *MNRAS*, 275, 255
- Thompson, C. & Duncan, R. C. 1996, *ApJ*, 473, 332
- Thompson, C., Lyutikov, M. & Kuikarni, S. R. 2002, *ApJ*, 574, 332
- Toll, J. S. 1952, Ph.D. Thesis, Princeton University
- Tsai, W. & Erber, T. 1974, *Phys. Rev. D* 10, 492
- Turolla, R., Zane, S. & Watts, A. L. 2015, *RPPH*, 78, 116901
- van der Horst, A. J., Kouveliotou, C., Gorgone, N. M., et al. 2012, *ApJ*, 749, 122
- Viganò, D., Rea, N., Pons, J. A., et al. 2013, *MNRAS*, 434, 123
- Wadiasingh, Z., Baring, M. G., Gonthier, P. L. & Harding, A. K. 2018, *ApJ*, 854, 95
- Wadiasingh, Z., Younes, G., Baring, M. G., et al. 2019, *arXiv:1903.05648*
- Wasserman, I. & Shapiro, S. L. 1983, *ApJ*, 265, 1036
- Younes, G., Baring, M. G., Kouveliotou, C., et al. 2017, *ApJ*, 851, 17
- Younes, G., Kouveliotou, C., van der Horst, A. J., et al. 2014, *ApJ*, 785, 52